



## RESEARCH ARTICLE

10.1029/2018JC014904

## A New Inverse Phase Speed Spectrum of Nonlinear Gravity Wind Waves

## Key Points:

- A spectrum representing wind waves as a function of their inverse phase speed is defined and examined using wave staff observations
- The new spectrum is consistent with the wavenumber spectrum for the shortest waves
- The inconsistencies observed in the frequency spectra are deduced to mainly be a result of wave nonlinearities

## Correspondence to:

J.-V. Björkqvist,  
jan-victor.bjorkqvist@fmi.fi

## Citation:

Björkqvist, J.-V., Pettersson, H., Drennan, W. M., & Kahma, K. K. (2019). A new inverse phase speed spectrum of nonlinear gravity wind waves. *Journal of Geophysical Research: Oceans*, 124, 6097–6119. <https://doi.org/10.1029/2018JC014904>

Received 23 DEC 2018

Accepted 3 AUG 2019

Accepted article online 7 AUG 2019

Published online 23 AUG 2019

Jan-Victor Björkqvist<sup>1</sup> , Heidi Pettersson<sup>1</sup> , William M. Drennan<sup>2</sup> , and Kimmo K. Kahma<sup>1</sup>

<sup>1</sup>Finnish Meteorological Institute, Helsinki, Finland, <sup>2</sup>Rosenstiel School of Marine and Atmospheric Science, University of Miami, Miami, FL, USA

**Abstract** The rear face of the wave spectrum is described by an equilibrium and a saturation subrange. Although accurate information about these ranges are highly relevant for wave modeling and many practical applications, there have been inconsistencies between results originating from temporal and spatial measurements. These discrepancies have been explained by the Doppler shift and the harmonics of nonlinear waves. We present high-frequency wave measurements from the Baltic Sea gathered with R/V *Aranda* using a wave staff array, which provided directional frequency-wavenumber data. In addition to the traditional wavenumber and frequency spectra,  $F(k)$  and  $S(\omega)$ , we also define a new spectrum that is a function of the inverse phase speed. We denote this spectrum  $Q(\nu)$ , where  $\nu = k\omega^{-1}$ . The properties of this  $Q$ -spectrum were studied using data from four different sites. A strongly forced fetch-limited case showed an equilibrium-to-saturation transition in the  $Q$ -spectrum, with less variations in the equilibrium constants compared to the frequency spectra. The transition to a saturation regime happened around  $U\nu = 3$  in all spectra where an equilibrium range was identified. Most duration-limited spectra had no equilibrium range in the inverse phase speed domain. The absence of an equilibrium range was consistent with the wavenumber domain, but the frequency spectra still showed an apparent equilibrium subrange extending to  $\omega U/g=5$ . The consistency of the saturation ranges between the  $Q$ -spectrum and the wavenumber spectrum indicate a weak Doppler shift effect. We deduced that the main factor distorting the frequency spectra was wave nonlinearities.

**Plain Language Summary** Surface waves are studied by partitioning them according to their length expressed in wave periods (seconds) or wavelengths (meters). Both approaches should give a similar descriptions of the waves, but in practice they produce inconsistent results. This limits our fundamental knowledge of waves and complicates practical applications. Measuring the wave period and the wavelength simultaneously is difficult, and there are not a lot of good data to study this problem. We measured the waves in the Baltic Sea from the ship R/V *Aranda* by recording the water level elevations using several thin submerged wires. From these observations we could describe the waves using both wave periods and wavelengths. The central part of our work was presenting the waves in a new way: We combined the wavelength and period measurements and partitioned the waves according to the speed which with they travel. The new partitioning shed light on the physical processes responsible for the discrepancies between the two traditional ways of representing the waves. This new approach might turn out to be useful, since many properties of the waves—such as the energy transfer from the wind—are controlled by their speed relative to the wind.

## 1. Introduction

Finding the proper description of wind generated surface waves is important for wave modeling, remote sensing, and air-sea interaction studies. Surface waves have traditionally been described by the variance density spectrum, either in the frequency or in the wavenumber domain. While real ocean waves are known to be nonlinear, the Fourier transform used to determine the wave spectrum still breaks down the data into linear components. One physical nonlinear wave in, for example, the frequency spectrum is thus described by its linear harmonics, which are indistinguishable from shorter free-traveling waves with the same frequency, but different phase speed.

Observed wave spectra, in particular, the frequency spectrum, contain significant contributions from nonlinear components that do not follow the linear dispersion (Donelan et al., 1985; Hara & Karachintsev, 2003;

©2019. The Authors.

This is an open access article under the terms of the Creative Commons Attribution License, which permits use, distribution and reproduction in any medium, provided the original work is properly cited.

Janssen, 2009; Leckler et al., 2015). In a study relying on Hamiltonian theory, Janssen (2009) determined the second-order correction to linear waves both in the wavenumber and frequency domain by including additional nonlinear terms that had not been accounted for in the previous studies of Barrick and Weber (1977) and Komen (1980). The author concluded that the second-order nonlinear effects were marginal in the wavenumber spectrum but distorted the higher part of the frequency spectrum. The results received experimental verification by Leckler et al. (2015).

What a nonlinear wave and its harmonics have in common is that they all travel with the same phase velocity—an obvious consequence of them collectively being one physical wave. This motivated us to define a new wave spectrum that is a function of the inverse phase velocity. For the approach to be fruitful, one needs to discard the assumptions relying on linear theory. In other words, we need to determine the frequency-wavenumber spectrum using spatiotemporal wave measurements. Such data can be extracted from, for example, marine radars (e.g., Lund et al., 2016) or stereo video footage (e.g., Leckler et al., 2015), and the latter technique has in later years led to studies of the directional frequency-wavenumber spectrum (Leckler et al., 2015; Peureux et al., 2018). Spatial and temporal wave data can also be acquired simultaneously using a large amount of wave staffs (Donelan et al., 1985). As shown by Donelan et al. (1996, 2015), even a smaller array is sufficient if the time series are processed using a tool suitable for nonstationary analysis, such as the Wavelet Directional Method (WDM; Donelan et al., 1996).

Regardless of the spectral domain, different regions of the wave spectrum above the spectral peak have long been described using two subranges: one wind-speed-dependent  $\omega^{-4}$  range, and one wind-speed-independent  $\omega^{-5}$  range ( $\omega$  is the wave frequency). Different theories for the mechanisms causing the apparent power laws in the respective subranges have been proposed (Banner, 1990; Kitaigorodskii, 1983; Phillips, 1958, 1985; Toba, 1973), but this fundamental question is not yet solved. Nevertheless, the existence of both subranges—and some kind of transition between them—has been established in several studies (e.g., Forristall, 1981; Kahma, 1981; Kahma & Calkoen, 1992; Lenain & Melville, 2017; Tamura et al., 2014). The names for these regions (the equilibrium/saturation range) have historically been used interchangeably to refer to either one (or both) of the subranges. We will henceforth call the wind-dependent  $\omega^{-4}$  region the *equilibrium range*. The  $\omega^{-5}$  region governing the shorter waves is referred to as the *saturation range*.

Theory predicts that there should be a connection between the subranges in the wavenumber and frequency domain, but field measurements have revealed inconsistencies where a transition to the saturation subrange is identifiable only in the wavenumber domain (Lenain & Melville, 2017). Interpreting frequency measurements are especially challenging since, compared to wavenumber measurements, they are more strongly affected by wave nonlinearities (Janssen, 2009). Moreover, they are also affected by the Doppler shift; the shorter waves are modulated by ambient currents, the wind induced drift, and the orbital motions of the longer waves (Banner, 1990; Guimarães, 2018; Kitaigorodskii et al., 1975; Leckler et al., 2015). We note that while the higher-order harmonics won't be separated from the dominant wave in the new inverse phase speed spectrum, it will also be modulated by currents.

In this study we aim to compare all three spectral representations of the wave field and have structured the paper as follows. In section 2 we describe the analysis methods and introduce the different spectra, while section 3 presents the experimental setup and available data. Section 4 starts by studying the saturation range in the wavenumber domain; any deviations from this constant in the new inverse phase speed measurements are expected to be caused mainly by the Doppler shift. The section continues with a presentation of the observed frequency spectra. Finally, we calculate the new inverse phase speed spectrum. The results are compared to the frequency spectra in an attempt to study the effect of wave non-linearities in the frequency measurements. We end by discussing and concluding our findings.

## 2. Analysis Methods

### 2.1. The Fourier Frequency Spectrum

We define dimensionless quantities for the frequency spectrum:

$$\tilde{\omega} = \omega U/g \quad (1)$$

$$\tilde{S}(\omega) = S(\omega)\omega^5/g^2 \quad (2)$$

$$\tilde{S}(\omega)\bar{\omega}^{-1} = S(\omega)\omega^4/(Ug), \quad (3)$$

where  $\omega = 2\pi f$  is the angular frequency,  $S(\omega)$  is the omnidirectional frequency spectrum, and  $U$  is the wind speed. We will call  $\tilde{S}(\omega)$  the frequency saturation spectrum and  $\tilde{S}(\omega)\bar{\omega}^{-1}$  the frequency equilibrium spectrum. The equilibrium spectrum is expected to be valid for certain subranges above the spectral peak, while the saturation spectrum is expected to describe the spectral region above the equilibrium range. These subranges are often displayed using their respective proportionality constants  $\alpha$  and  $\alpha_u$ :

$$S(\omega) \sim \alpha g^2 \omega^{-5} \quad (4)$$

$$S(\omega) \sim \alpha_u U g \omega^{-4}, \quad (5)$$

where the wind speed ( $U$ ) can be given as, for example, the mean 10-m wind speed ( $U_{10}$ ), or the friction velocity ( $u_*$ ).

## 2.2. The WDM

The WDM (Donelan et al., 1996) is a tool for nonstationary wave analysis. The WDM gives information about the wave energy as a function of time and frequency (actually scale). If data from at least three different wave staffs are available, the phase lags between the staffs also determine the wavenumber,  $k$ , and the direction,  $\theta$ , of the waves.

We determined the directional frequency spectrum  $S(\omega, \theta)$  ( $\text{m}^2/\text{Hz}/\text{rad}$ ) by binning the variance in each time and frequency bin with respect to the direction.

### 2.2.1. Wavenumber Spectrum

By binning the variance with respect to the wavenumber and the direction, we obtained the directional wavenumber spectrum  $\Psi(\mathbf{k}) = \Psi(k, \theta)$  ( $\text{m}^4/\text{rad}$ ).

The omnidirectional wavenumber spectrum,  $F(k)$  ( $\text{m}^3$ ), is determined as

$$F(k) = \int_{-\pi}^{\pi} \Psi(k, \theta) k \, d\theta. \quad (6)$$

The frequency–wavenumber spectrum  $\mathbb{F}(\mathbf{k}, \omega) = \mathbb{F}(k, \omega, \theta)$  ( $\text{m}^4/\text{Hz}$ ) and its omnidirectional form  $\int_{-\pi}^{\pi} \mathbb{F}(k, \omega, \theta) k \, d\theta$  ( $\text{m}^3/\text{Hz}$ ) were determined by a similar binning technique.

We define dimensionless quantities for the wavenumber spectrum:

$$\tilde{k} = kU^2/g \quad (7)$$

$$B(k) = F(k)k^3, \quad (8)$$

where  $B(k)$  is the wavenumber saturation spectrum. As with the frequency spectrum, both the saturation and the equilibrium ranges can be presented using proportionality constants

$$F(k) \sim \frac{\alpha}{2} k^{-3} \quad (9)$$

$$F(k) \sim \frac{\alpha_u}{2} U g^{-0.5} k^{-2.5}, \quad (10)$$

where  $\alpha$  and  $\alpha_u$  are the constants of the frequency spectrum introduced above (see, e.g., Kitaigorodskii, 1983).

### 2.2.2. Wave Spectrum as a Function of the Inverse Phase Speed

It is possible to assign each wave component a phase speed if both the wavenumber and the frequency are measured. This is the case when using, for example, the WDM, which can resolve waves with the same frequency, but different wavenumbers. Nevertheless, we will replace the phase speed with the inverse phase speed,  $\nu = c^{-1}$ , to regain an orientation familiar from traditional wave spectra.

We normalize this new directional spectrum in a similar fashion to the wavenumber domain such that

$$Q(\nu) = \int_{-\pi}^{\pi} \mathcal{Q}(\nu, \theta) \nu \, d\theta \quad (11)$$

$$\nu = \frac{\mathbf{k}}{\omega} \quad (12)$$

**Table 1**  
*Wind and Wave Conditions for the Different Sites*

Run ID	Depth (m)	Length (h)	Date	$H_s$ (m)	$U_{10}$ (m/s)	$U/c_p$ (-)
15031	68	6.0	08 July 2015	0.61–0.71	1.7–7.0	0.16–0.99
15033	25	3.5	09 July 2015	0.28–0.35	6.1–9.6	1.51–2.88
15034	122	5.5	10 July 2015	0.32–0.43	1.5–6.3	0.29–1.93
15035	122	6.0	10 July 2015	0.47–1.49	6.2–8.8	0.82–1.88
15040	235	4.0	13 July 2015	0.55–0.76	0.0–2.3	0.00–0.33
15042	159	1.5	13 July 2015	0.27–0.32	1.6–2.1	0.26–0.34
15043	121	1.0	13 July 2015	0.26–0.29	0.6–0.7	0.11–0.13
15044	35	5.0	14 July 2015	0.21–0.29	1.7–3.3	0.30–0.61

*Note.* The length in hours refers to the length of the measurement time series.

$$\nu = |\nu|, \quad (13)$$

where  $\nu$  is the inverse phase velocity and  $\nu$  is its modulus,  $Q(\nu, \theta)$  ( $\text{m}^4/(\text{s}^2\text{rad})$ ) is the directional spectrum, and  $Q(\nu)$  ( $\text{m}^3/\text{s}$ ) is the omnidirectional spectrum. We will henceforth call the omnidirectional version of this new spectrum the inverse phase speed spectrum or the  $Q$ -spectrum.

To our knowledge this kind of spectrum has not previously been formally defined and examined. To provide the reader with some intuition we note that for linear waves in deep water  $\nu = c^{-1} = \omega g^{-1}$ . This also means that the inverse phase speed spectrum adds no new information unless frequency-wavenumber measurements provide the true phase speed of the waves.

The omnidirectional  $Q$ -spectrum has dimensionless forms corresponding to  $\nu^{-4}$  and  $\nu^{-5}$  power laws, which are analogous to the regimes in the frequency spectrum; the former is a wind speed-dependent equilibrium range, while the latter is a saturation range scaling only with the gravitational acceleration. Since the normalization of the directional  $Q$ -spectrum is similar as for the wavenumber spectrum, one directional slice might be expected to follow a  $\nu^{-6}$  power law (cf. a  $k^{-4}$  slice in the wavenumber domain). The directional properties of the  $Q$ -spectrum will, however, not be the focus of this paper.

As with the frequency and wavenumber spectra, we can define dimensionless quantities

$$\tilde{\nu} = \nu U \quad (14)$$

$$\tilde{Q}(\nu) = Q(\nu)\nu^5 g^2 \quad (15)$$

$$\tilde{Q}(\nu)\tilde{\nu}^{-1} = Q(\nu)\nu^4 g^2 / U, \quad (16)$$

where  $\tilde{\nu}$  is merely  $U/c$ . The two spectra resemble the saturation and equilibrium spectra of the frequency domain in a natural way with the same proportionality constants  $\alpha$  and  $\alpha_u$ :

$$Q(\nu) \sim \alpha g^{-2} \nu^{-5} \quad (17)$$

$$Q(\nu) \sim \alpha_u U g^{-2} \nu^{-4}. \quad (18)$$

### 3. Data

#### 3.1. Experimental Setup

The data were collected in the Baltic Sea during R/V *Aranda*'s research expedition in July 2015. The Baltic Sea is a semienclosed basin with a mean depth of about 50 m. The longest fetches, of around 700 km, are found in the Baltic Proper. The shorelines are complex and often have dense archipelagos—especially the Finnish coastline in the north. Table 1 and Figure 1 provides an overview of the eight measurement runs that form the data set for this study. Each run is denoted with an index from 15031 to 15044.

R/V *Aranda* was aligned with the wind in the beginning of each measurement. If the discrepancy between the wind direction and ship direction grew too large (greater than  $\sim 20^\circ$ ), the ship direction was slowly

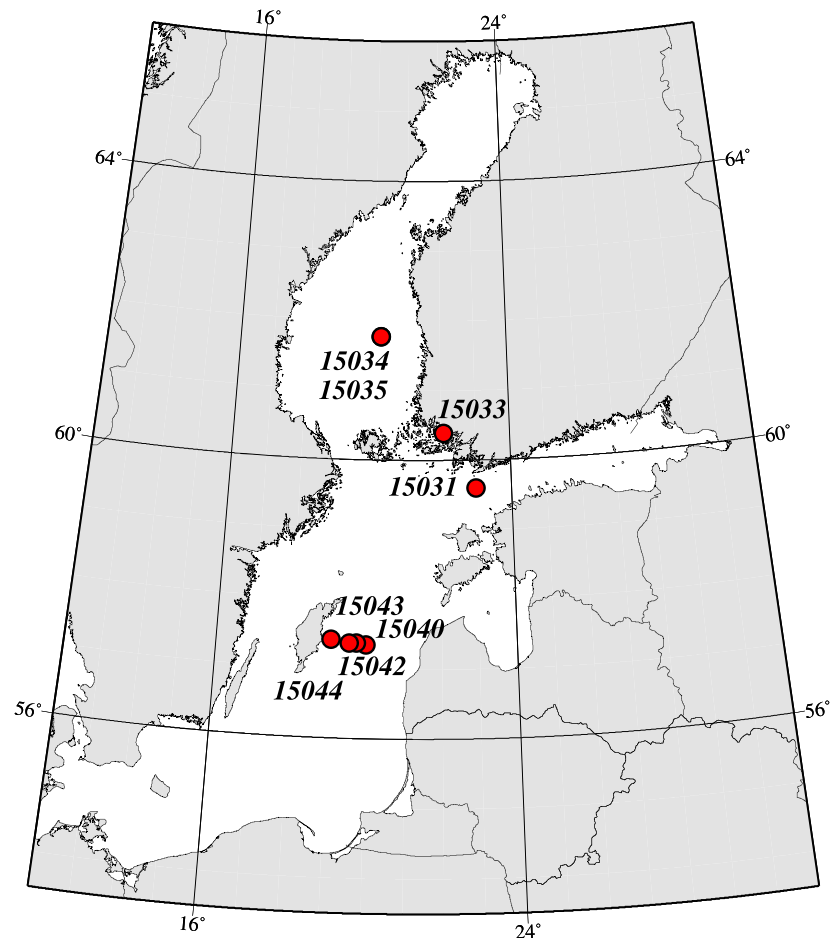


**Figure 1.** Measurement locations for the 2015 R/V *Aranda* summer expedition.

realigned with the wind. During Runs 15040 and 15044 the ship was aligned with the swell, since the wind was very weak (0–2 m/s) with a varying direction.

The full ship motion (6 degrees of freedom) was registered by an MRU6 (Motion Reference Unit). Following Drennan et al. (1994), a full correction for the movement of the ship was applied to both the wind and the wave measurements.

### 3.2. Wave Measurements

We conducted wave measurements with a wave staff array submerged in front of the bow of a stationary R/V *Aranda* (Figure 2). The array had five wave staffs fixed 25 cm apart in the shape of a plus sign. For Run 15042 the wave staffs were 15 cm apart and the middle staff was removed. A 24-bit QuantumX AD converter equipped with a Bessel antialiasing filter sampled the data at 200 Hz.

The voltage logged by the capacitive wave staffs were transformed to water level elevations by multiplying with a calibration coefficient. Some of the wave staffs were calibrated statically, while the rest were calibrated dynamically by matching the variance to a statically calibrated wave staff.

We calculated the omnidirectional frequency wave spectra from 30-min surface level elevation data of a single wave staff. The time series were tapered by a Blackman-Harris window, and the final wave spectra were calculated by averaging elementary bins of the raw fast Fourier transform spectra. The final spectra had a frequency resolution of  $\Delta\omega = 0.1\pi$  rad/s up to  $\omega = 2\pi$ , and a resolution of  $\Delta\omega = 0.2\pi$  rad/s above that.

An example of wave spectra is given in Figure 3a. The wave staff array registered data near Finnish Meteorological Institute's Bothnian Sea wave buoy (Runs 15034 and 15035), and the wave buoy near the island Gotland in the Baltic Proper (Run 15044; Figure 1). Both buoys were accelerometer-based Datawell

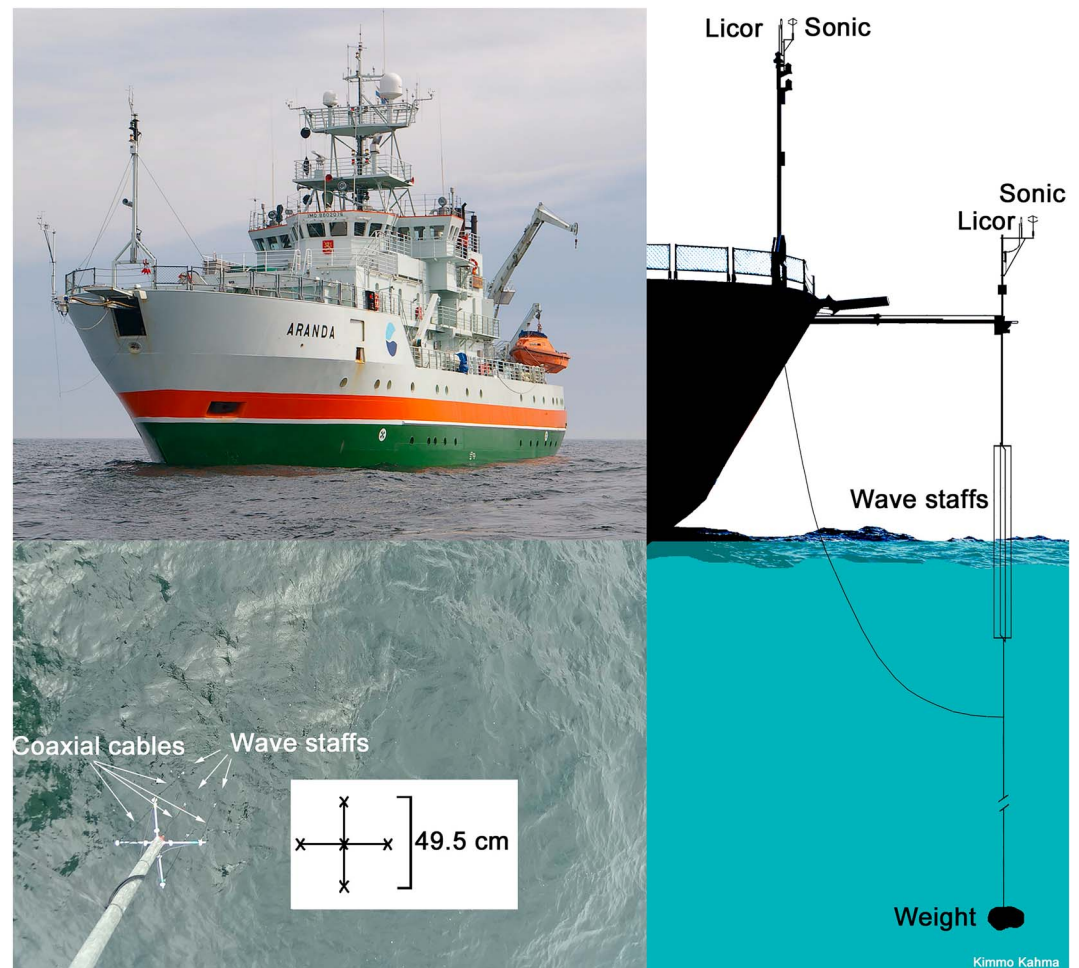


**Figure 2.** A slightly older version of the experimental setup on R/V *Aranda* (top left). The wave staff array used in this study (bottom left). A schematic picture over the current experimental setup (right).

Directional Waveriders (Mk-III). The wave spectra calculated from the wave staff data were found to be in good accord with the wave buoy spectra (Figure 3).

The peak frequency was calculated by a parabolic fit from a spectra where only 31 elementary bins had been averaged to increase the frequency resolution near the spectral peak. The significant wave height  $H_s = H_{m_0}$  was calculated using an upper integration limit of  $20\pi$  rad/s (10 Hz).

### 3.2.1. Wave Data From the Array

We used the WDM to analyze the simultaneous data from all five wave staffs in the array. The implementation relied on the code by Donelan et al. (1996, 2015), with minor modifications.

Prior to the application of the WDM we applied a Gaussian filter (25-ms standard deviation and 405-ms window length) and downsampled the time series to 25 Hz in order to avoid interpreting high-frequency noise as true water level differences. To minimize spatial aliasing, we also did not use wave staff pairs with a distance greater than 25 cm. The four remaining 25-cm pairs (see Figure 2) gave four estimates of the wavenumber and direction at each time and frequency, which we consequently averaged.

We used four voices in addition to the base Morlet wavelets, resulting in 15 logarithmically spaced angular frequencies (scales) between  $0.25\pi$  and  $6.35\pi$  rad/s. In practice, we determined the final spectra by binning the variance as a function of the other desired variables (wavenumber  $k$ , inverse phase speed  $\nu$ , and/or direction  $\theta$ ). The directional spectra were binned with a resolution  $\Delta\theta = 10^\circ$ . The wavenumbers and inverse phase speeds were binned with resolutions of  $\Delta k = 1/12$  rad/m  $\Delta\nu = 1/50$  s/m. We only used wavenumbers less than 9 rad/m in the binning of the inverse phase speed spectrum because of the high noise close to the Nyquist wavenumber.

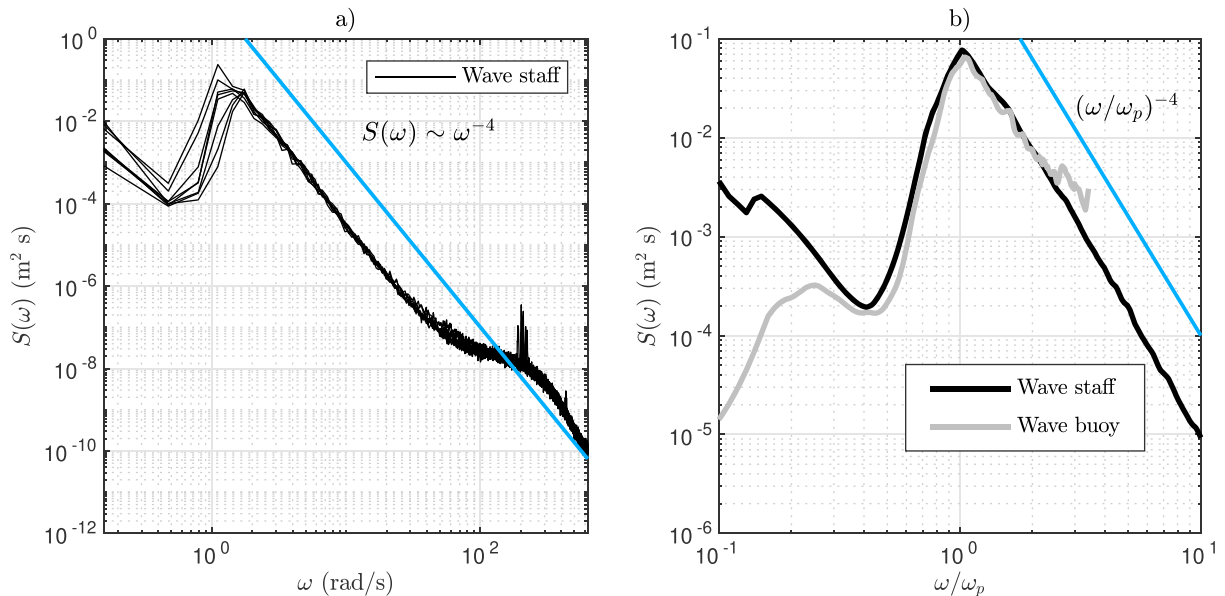


**Figure 3.** (a) The evolution of the wave spectrum at location 15035 over 4 hr (2015-07-10T14:39 to 2015-07-10T18:09). (b) The average spectrum calculated from the wave staff (black) and a wave buoy located 3.5 km upwind (gray). The blue line shows an  $\omega^{-4}$  power law.

### 3.3. Wind Measurements

Sonic anemometers (Metek USA-1) installed at 10.1 and 16.2 m above sea level provided eddy-covariance measurements. The lower device was mounted on a horizontal boom projecting from the bow of the ship, while the other anemometer was installed at the top of a mast near the edge of the bow. Two  $CO_2/H_2O$  gas analyzers—an open path LI-COR (LI-7500) and an enclosed path LI-COR (LI-7200)—were installed at both heights and provided humidity fluxes. All six devices were sampled at 10 Hz. An overview of the experimental setup is shown in Figure 2.

In this paper we used the measurements from the height of 10.1 m. Numerical flow modeling, wind tunnel measurements with a scaled ship model, and field comparisons have all consistently shown the wind speed measurements at this height to be 6% too low when the bow was within  $\pm 20^\circ$  into the wind direction. This bias was corrected in the mean wind speed, which we calculated as 30-min averages.

The friction velocity  $u_*$  was determined from the time series assuming that the stress and wind vectors are aligned:

$$u_* = \left( -\overline{u'w'} \right)^{\frac{1}{2}}, \quad (19)$$

where  $\overline{u'w'}$  is the momentum flux in the along wind direction. Comparison measurements have indicated that the flow distortion effects on turbulence are within error limits, which is why we used the friction velocity as is, following Dupuis et al. (2003)

### 3.4. Weather Conditions

The data set of this study consists of observations made from R/V *Aranda* in the Baltic Sea. The wind conditions varied between 0 and 10 m/s, and the significant wave height ranged from 0.2 to 1.5 m. A numerical overview is available in Table 1, and the measurement locations can be found in Figure 1. We will now briefly introduce the different runs.

**15031 (Gulf of Finland):** A 0.2-Hz swell propagated from  $240^\circ$  to the entrance of the Gulf of Finland. A southerly wind rose during the first hours, with the wind speed finally staying between 5 and 7 m/s for 5 hr. The wind gradually turned toward the southeast, where the fetch was around 60 km. The significant wave height stayed between 0.6 and 0.7 m, while the inverse wave age,  $U/c_p$ , fluctuated around 0.8 because of the swell.

**15033 (Archipelago Sea):** The wind speed was initially 9–10 m/s, but slowly decayed to 6 m/s while maintaining a direction around  $200^\circ$ . The fetch to the nearest island was about 2 km, but

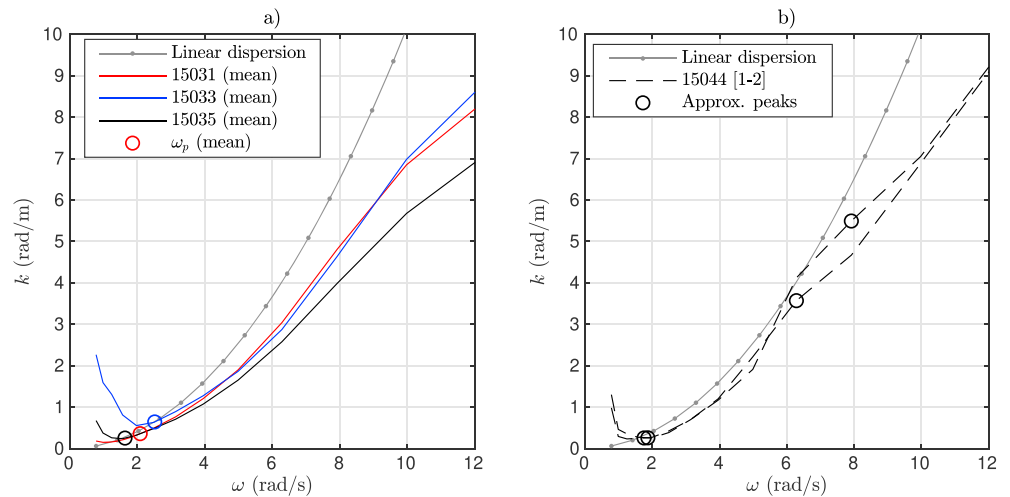


**Figure 4.** The measured dispersion relation. The solid lines (a) shows the mean values ( $U/c_p > 0.8$ ) of the dispersion curves calculated for three different runs, and the circles denote the mean of the peak frequencies. The dashed lines (b) show the dispersion curves determined from a two 30-min time series where the spectrum is double peaked. The black circles are the spectral peaks approximated from the Wavelet Directional Method spectrum. The gray dotted line is the theoretical linear dispersion curve.

a narrow passage in the southern direction had a fetch around 14 km. The waves were strongly forced ( $U/c_p = 1.5\text{--}2.9$ ).

**15034 (Bothnian Sea):** During the first 3 hr the wind speed was less than 3 m/s and the waves were swell ( $U/c_p \sim 0.3$ ). By the time the inverse wave age exceeded 0.8 the wind had turned from the east to the north. The northerly wind kept rising, ending up at 6 m/s.

**15035 (Bothnian Sea):** 15035 was from the same location as the previous run, and directly followed it. A northerly duration-limited wave system developed. The wind speed was 7–8 m/s the first 3 hr; the significant wave height grew from 0.5 to 0.9 m. After a 1-hr dip to 6 m/s, the wind speed continued at 8–9 m/s for two more hours, finally growing the significant wave height to 1.5 m and the peak frequency to 0.2 Hz. The inverse wave age was between 0.8 and 1.9.

**15040 (Baltic Proper):** With no wind for the first two and a half hours, R/V *Aranda* was aligned with a 0.2-Hz northerly swell. For the last hours a 2-m/s northerly wind generated a 1.5-Hz wind sea.

**15042 (Baltic Proper):** This station was located 15 km west of 15040. The main part of the wave field was a 0.3 m northerly swell at 0.2–0.3 Hz, resulting in an inverse wave age of 0.3. The speed of the northerly wind was 2 m/s.

**15043 (Baltic Proper):** This 1-hr measurement was made 12 km west of 14042. The same northerly swell still dominated; the wind speed was below 1 m/s.

**15044 (Gotland):** The wind speed from the east and north-east was 2–3 m/s. The dominant wave system was a 0.2 m swell at 0.2–0.3 Hz coming from north-north-east. The wind sea evolved from 1.5 Hz to around 0.6 Hz over the course of 6 hr; the total significant wave height rose to 0.3 m. The inverse wave age was constantly below 0.8 because of the swell, but the wind sea was actively forced the entire time.

## 4. Results

### 4.1. The Dispersion Relationship and Directional Properties

In Figure 4a we show the measured mean dispersion relation for three stations that have the highest wind speeds and most well-defined conditions. The duration-limited case (15035) differ more from the linear relation compared to the fetch-limited cases (15031 and 15033). A comparison between runs 15031 and 15033 also show that the deviation from the linear dispersion is not tied to a certain multiple of the peak

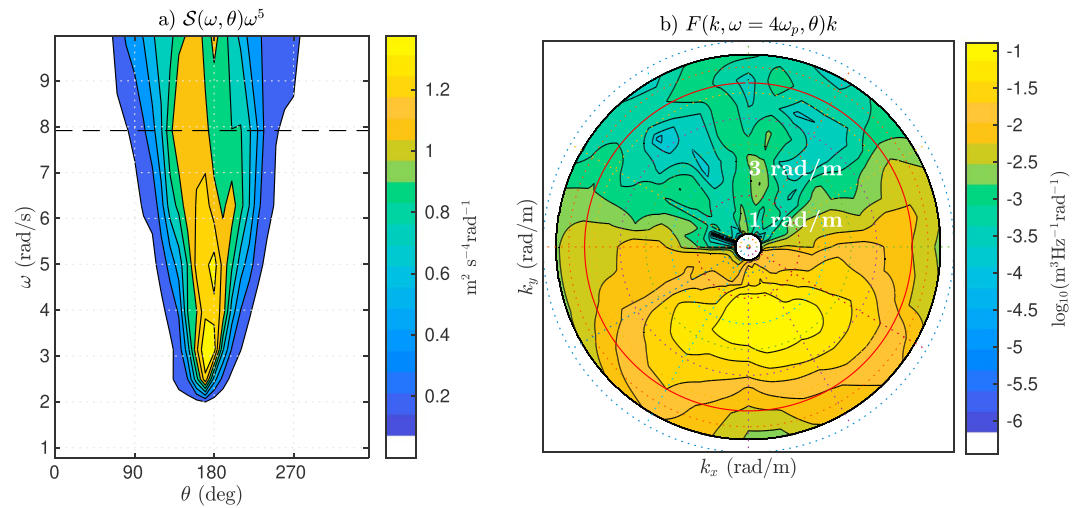


**Figure 5.** The directional frequency spectrum multiplied by  $\omega^5$  (a) and a frequency slice  $\mathbb{F}(k, \omega=4\omega_p, \theta)k$  (b) as seen by the Wavelet Directional Method (spectrum 15035 [1]). The black dashed line marks  $\omega=4\omega_p$ . The red line marks the linear dispersion shell.

frequency, since their mean dispersion curves overlap for higher frequencies even though their mean peak frequency differ. The variance with respect to the peak can also readily be seen from run 15031, where the mean value of the peak frequency is closer to that of run 15035, but the mean dispersion curve for the higher frequencies is close to that of 15033. Figure 4b illustrates the dispersion relation determined from individual spectra that have a peak frequency of 2 rad/s and a wind sea peaks at around 6–8 rad/s ( $U_{10} = 2\text{--}3$  m/s). The dispersion curves at both peaks are very close to the linear dispersion relation. The instability of the higher peak is mainly because of the limited frequency resolution in the WDM spectrum.

A deviation from the linear dispersion relation has been found by several authors (e.g., Donelan et al., 1985, 2015; Hara & Karachintsev, 2003; Wang & Hwang, 2004) and the nonlinearities have been explained to be caused by bound harmonics. If the full direction frequency-wavenumber spectrum is available, these harmonics should be visible by examining all the wavenumbers at a certain frequency. This was done explicitly by Leckler et al. (2015) and Peureux et al. (2018). The energy of wave components having different wavenumbers (but the same frequency) are also distinguishable in our measurements, although both the measurement technique and our analyzing method are different (Figure 5b).

#### 4.2. Wavenumber Saturation Spectrum

We grouped the saturation spectra,  $B(k)$  (equation (8)), according to the wind speed, and each spectrum in Figure 6a thus represents one group average. The individual spectra are shown in Figure 6b. Most averaged spectra have a  $B(k) \propto k^{0.5}$  equilibrium slope before saturating at the higher wavenumbers. In the equilibrium regime the wave energy increases with the wind speed, but the saturation collapse the spectra to a value of  $B(k)=5\text{--}6 \cdot 10^{-3}$ . For wind speeds under 3 m/s the saturation range is not captured in the measurements because of limitations in the wave staff spacing. The  $k^{0.5}$  slope is still visible, with the exception of the 0- to 1-m/s group. Nevertheless, the scatter in the lower wind speed bins is large (Figure 6b).

An averaging effect is also seen for the wind speed bin 4–5 m/s, where an equilibrium range is present for two individual spectra, but absent in the average. These spectra belong to run 15034, where the wind turns, thus resulting in a swell not aligned with the wind.

The data consist of measurements from different geographical conditions (see Figure 1). We therefore decided to treat the three main sites with the highest wind speeds (15031, 15033, and 15035) separately, while using the dimensionless wavenumber  $\tilde{k} = kU^2/g$  to compare spectra from different wind conditions. Because of the measurement noise caused by the limitations in the wave staff spacing, wavenumbers greater than 4 rad/m were discarded, along with data below the spectral peak  $k_p$ .

Spectra in both 15031 and 15033 transition from the equilibrium to the saturation regime at about  $\tilde{k} = 10$ , with saturation values near  $6 \cdot 10^{-3}$  (Figures 7a and 7b). For 15035 the equilibrium regime is visible at

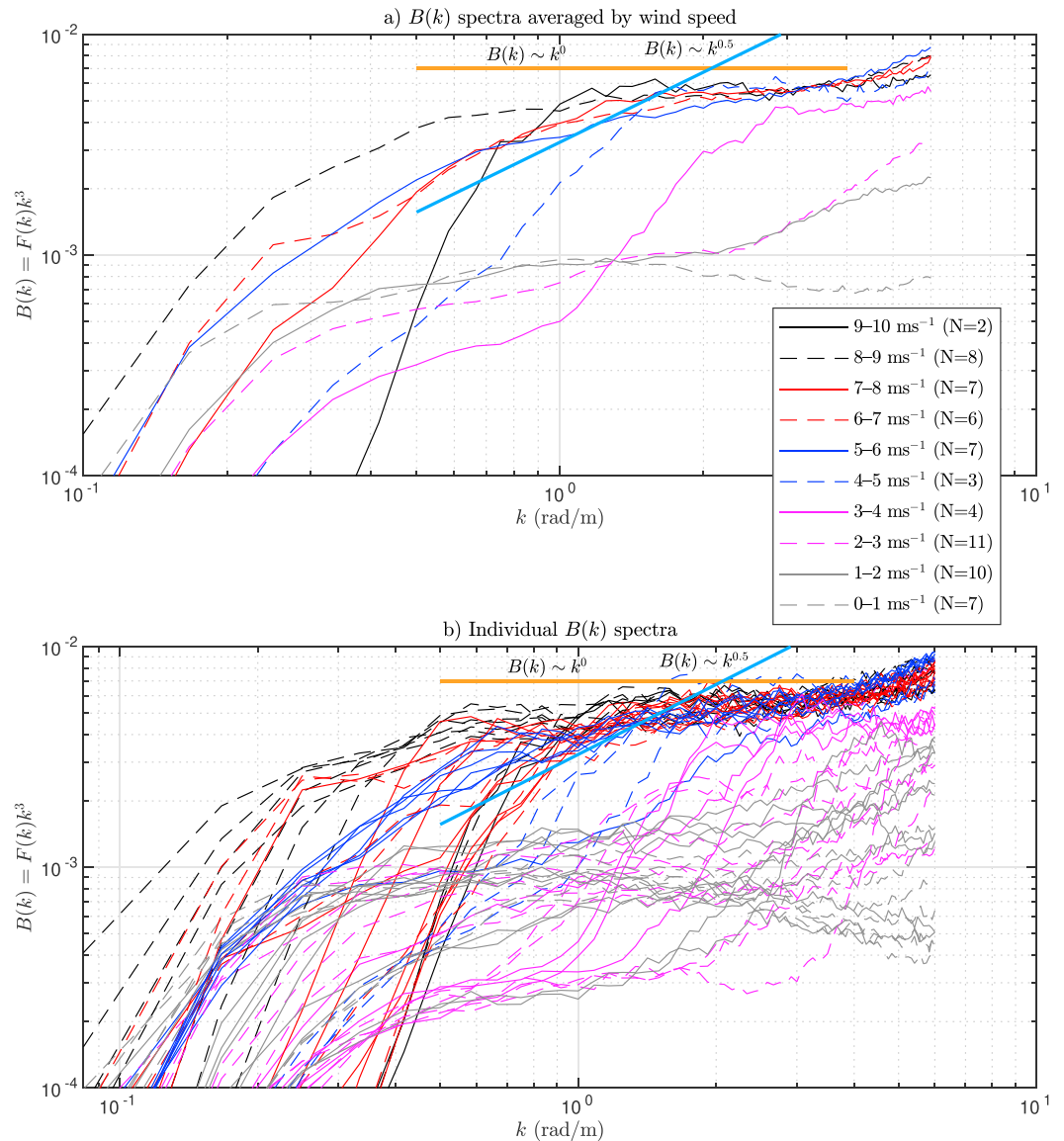


**Figure 6.** Saturation spectra  $B(k) = F(k)k^3$  for different ranges of the wind speed (a). The individual spectra are shown in panel (b).

$2 < \tilde{k} < 4$ , but the transition is less clear. The dimensionless wavenumber collapses the spectra also in the equilibrium regime, a feature especially visible for run 15035.

The spectra calculated using the combined data from all three aforementioned runs collapse well, although the limited amount of data causes some instability in the mean spectra (Figure 8a). After the equilibrium-to-saturation transition at around  $\tilde{k} = 10$  this composite data set saturates to  $B(k) = 5.8 \cdot 10^{-3}$ , which means that the Phillips' constant would have a value of  $\alpha = 1.2 \cdot 10^{-2}$ .

The dimensionless wavenumber can also be defined using the friction velocity, that is, as  $k^* = ku_*^2/g$ . Scaling with the friction velocity also produces a coherent group of spectra saturating at higher values of  $k^*$  (Figure 8b). It is challenging to determine an exact point of transition between the regimes, but it falls in the range of  $k^* = 0.01\text{--}0.02$ . This transition point is in line with the findings of Lenain and Melville (2017), whose results show an equilibrium range extending to  $k^* \approx 0.01$ .

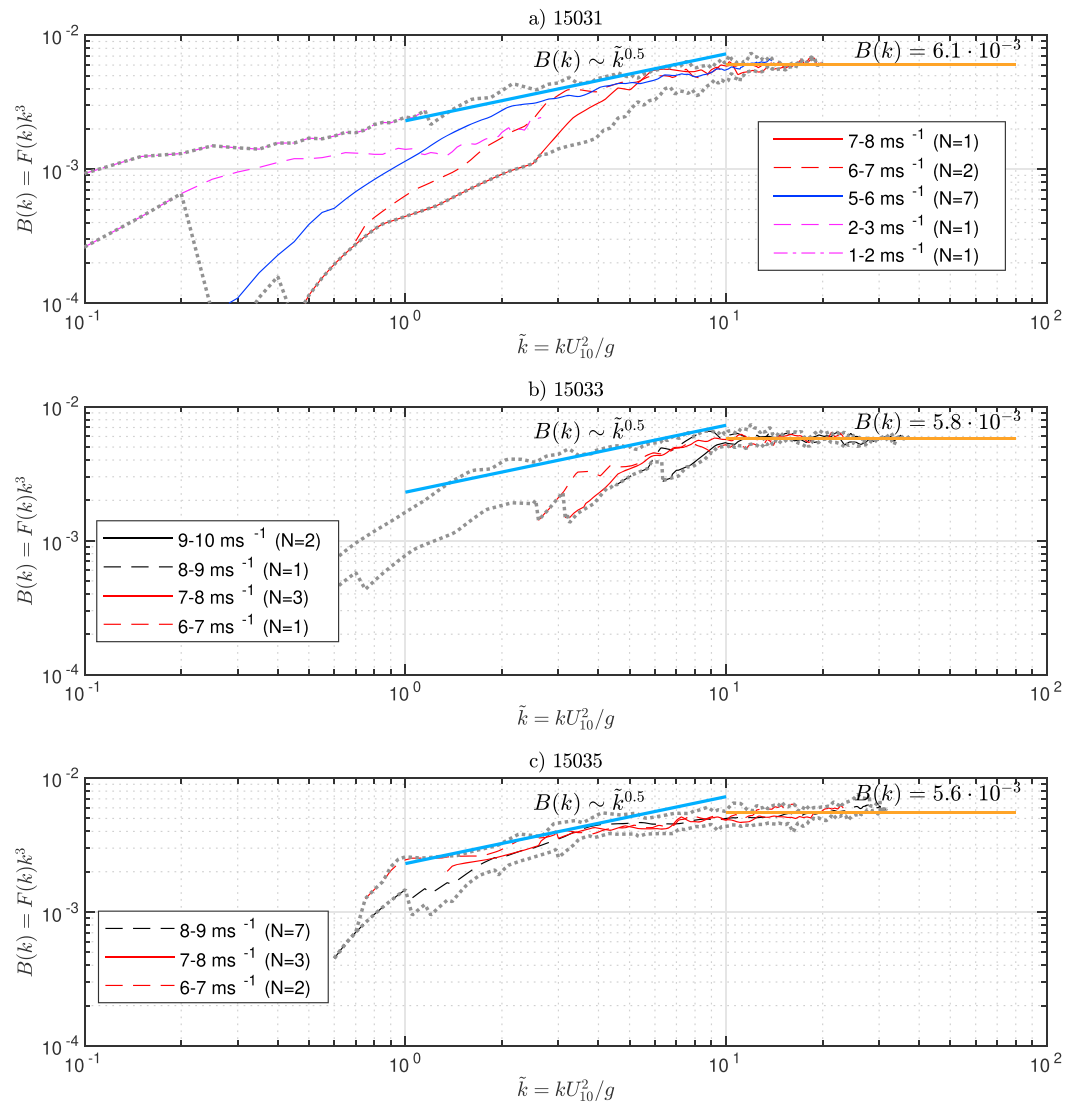


**Figure 7.** Saturation spectra  $B(k)=k^3F(k)$  as the function of the dimensionless wavenumber at three different sites (a–c). The gray dotted lines mark the maximum and minimum values of individual spectra. Only wavenumbers  $k_p \leq k \leq 4$  rad/m are included in the average.

### 4.3. Frequency Equilibrium Spectrum

We grouped the equilibrium spectra  $S(\omega)\omega^4/(Ug)$  according to the wind speed. Situations with an inverse wave age under 0.8 were excluded, as were frequencies below the spectral peak. Data from each group formed a mean spectrum representative for that wind speed range, which we plotted as a function of two nondimensional angular frequencies,  $\tilde{\omega} = \omega U/g$  and  $\omega/\omega_p$  (Figure 9).

As a function of  $\tilde{\omega}$  the spectra show two  $\omega^{-4}$  power law regions (Figure 9a). The equilibrium range extend from roughly  $\tilde{\omega}=1-2$  to  $\tilde{\omega}=4-5$ , and its equilibrium level is in line with  $\alpha_u = 4.5 \cdot 10^{-3}$  (found by Kahma, 1981). The only outlier is the highest wind speed class (9–10 m/s, solid black). A connection to the strength of the forcing (as proposed by Donelan et al., 1985) can be seen when the spectra are binned with respect to the inverse wave age instead of the absolute wind speed (Figure 9c). An increased forcing lowers the equilibrium level and increases the transition frequency. As the second  $\omega^{-4}$  range will not be considered in this paper, we simply note in passing that it ranges from approximately  $\tilde{\omega} = 10$  to at least  $\tilde{\omega} = 20$ ; this is well beyond what we can resolve in the wavenumber domain.

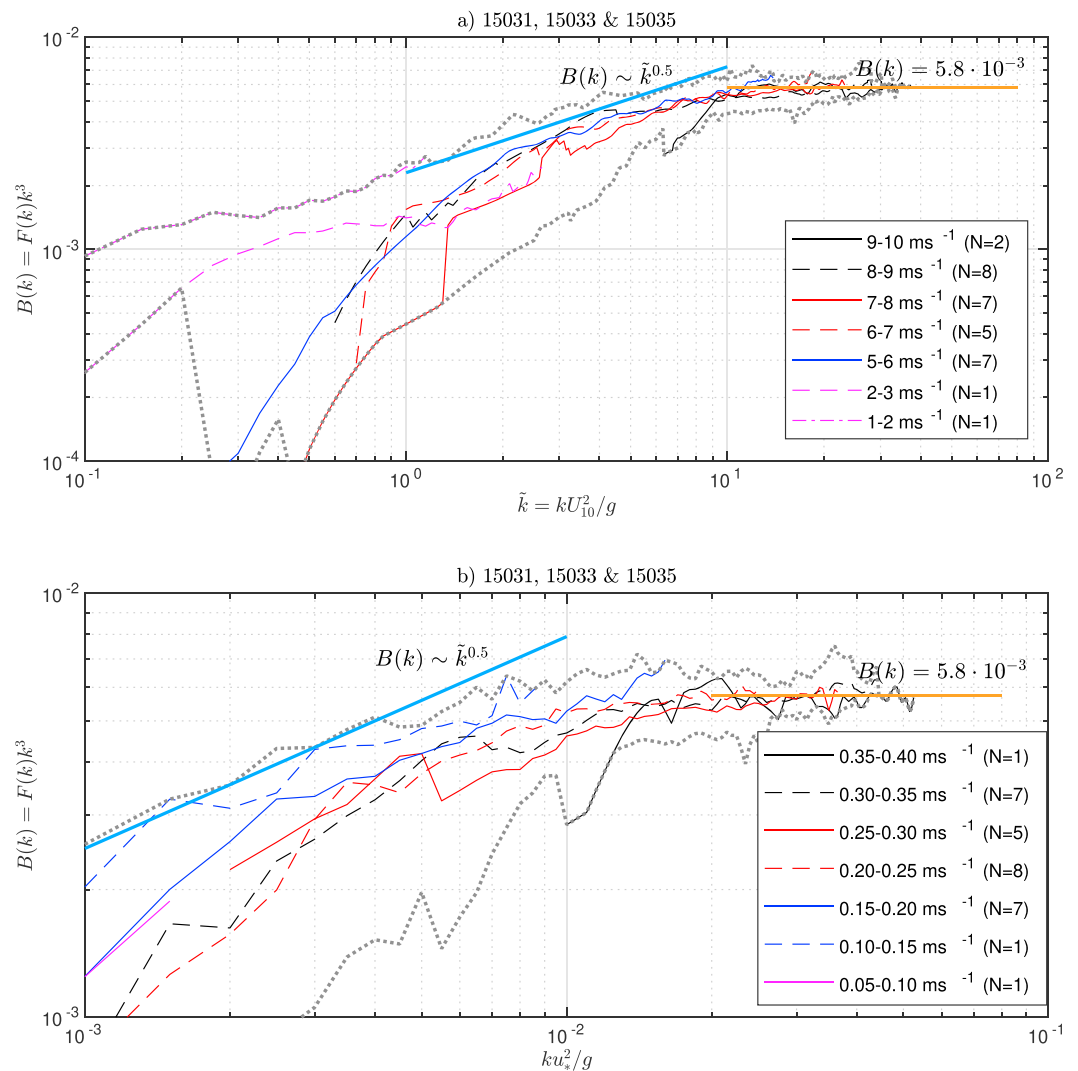


**Figure 8.** Saturation spectra  $B(k)=k^3F(k)$  from sites 15031, 15033, and 15035 as the function of the dimensionless wavenumbers (a)  $kU_{10}^2/g$  and (b)  $ku_*^2/g$ . The gray dotted lines mark the maximum and minimum values of individual spectra. Only wavenumbers  $k_p \leq k \leq 4$  rad/m are included in the average.

Although the transition point between the different regimes cannot be determined unequivocally, most of the spectra show a shift around  $\tilde{\omega} = 4-5$ , which is consistent with  $\tilde{\omega} = 5$  determined by Kahma and Calhoun (1992). The two  $\omega^{-4}$  ranges are connected by a transition slightly slower than  $\omega^{-5}$ . Banner (1990) attributed the deviation from the  $\omega^{-5}$  form of Phillips (1958) to the Doppler shift, but later studies have determined that this effect is relatively small (Guimarães, 2018; Leckler et al., 2015; Peureux et al., 2018), and the presence of nonlinear harmonics have been offered as the explanation (e.g., Hisaki & Tokuda, 1995; Janssen, 2009).

The picture is less clear when the frequencies are scaled with respect to  $\omega_p$  (Figure 9b). For the highest wind speeds ( $U > 7$  m/s) it is possible to interpret the spectra to have an equilibrium range ending at  $3\omega_p$ . Still, for the wind speeds 4–6 m/s the equilibrium range seems to extend to  $5-6\omega_p$ . When binned with respect to the inverse wave age (Figure 9d), a somewhat consistent transition is visible around  $3-4\omega_p$ , which is in line with Banner (1990).

In summary, while different parts of our results do not directly contradict previous findings of Kahma (1981), Donelan et al. (1985), and Banner (1990), none of the four representations in Figure 9 can provide a comprehensive description of the frequency spectra. Our data seem to be best explained by the assumptions in panel (c), namely, that there exist a fixed saturation level ( $\alpha \approx 2.5 \cdot 10^{-2}$ ) and that the equilibrium level depends on the strength of the forcing.

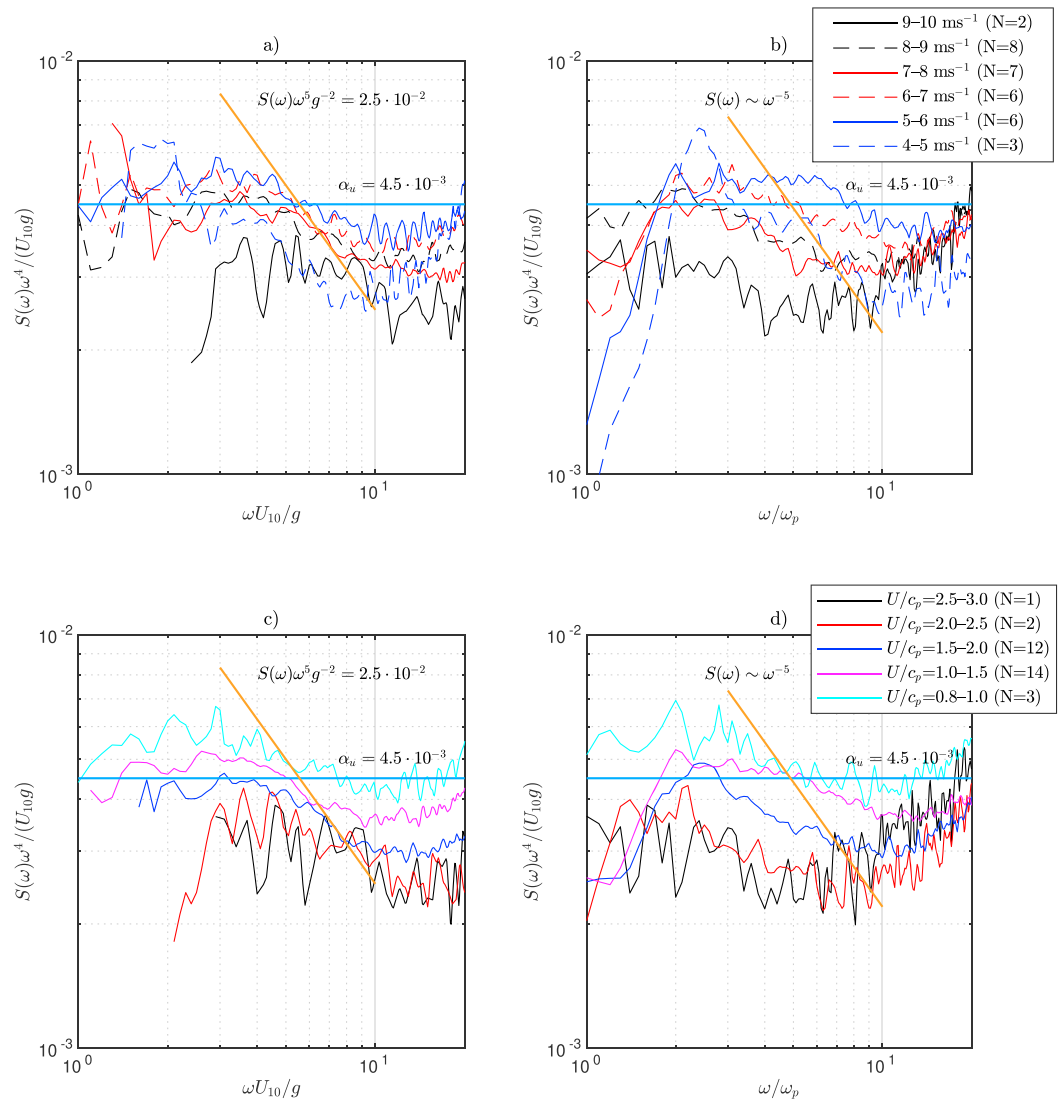


**Figure 9.** Equilibrium spectra  $S(\omega)\omega^4/(U_{10}g)$  classified according to the wind speed (a, b) and the wave age (c, d) as a function of the dimensionless angular frequencies  $\omega U/g$  (a, c) and  $\omega/\omega_p$  (b, d). In both plots only cases where  $U/c_p > 0.8$  are accepted and frequencies  $\omega < \omega_p$  are discarded from the spectral averages.

#### 4.4. Inverse-Speed Spectrum $Q(v)$

In deep water the dimensionless frequency,  $\omega U/g$ , and the dimensionless wavenumber,  $kU^2/g$ , are often interpreted as the inverse wave age,  $U/c$ , or as  $(U/c)^2$ , respectively. Such an interpretation, however, assumes that every wave component obeys the linear dispersion relation. Because of wave nonlinearities, this is a poor assumption especially in the rear face of the frequency spectrum. Although not easily defined using traditional frequency measurements, the relation between the phase speed of the wave component and the wind speed is still a central quantity. To examine this aspect without being bound by the assumptions of linear theory, we defined a spectrum using the measured phase speed of the wave components.

Example spectra of a strongly forced, fetch-limited case is presented in Figure 10. The omnidirectional inverse phase speed spectrum (a) shows a transition from the  $v^{-4}$  equilibrium subrange to the  $v^{-5}$  saturation subrange at about  $v = 0.4$  s/m. The omnidirectional wavenumber spectrum (b) shows  $k^3$  the saturation range already identified in Figure 7b, but the existence of a  $k^{2.5}$  region is less clear. The inverse phase speed spectra estimated from  $S(\omega)$  and  $F(k)$  using linear theory shows that the  $Q$ -spectrum is not merely a rescaling of the traditional spectra (a). Unsurprisingly, the disagreement is largest for the short waves in spectrum estimated from the frequency measurements. Although directional properties are not discussed in more

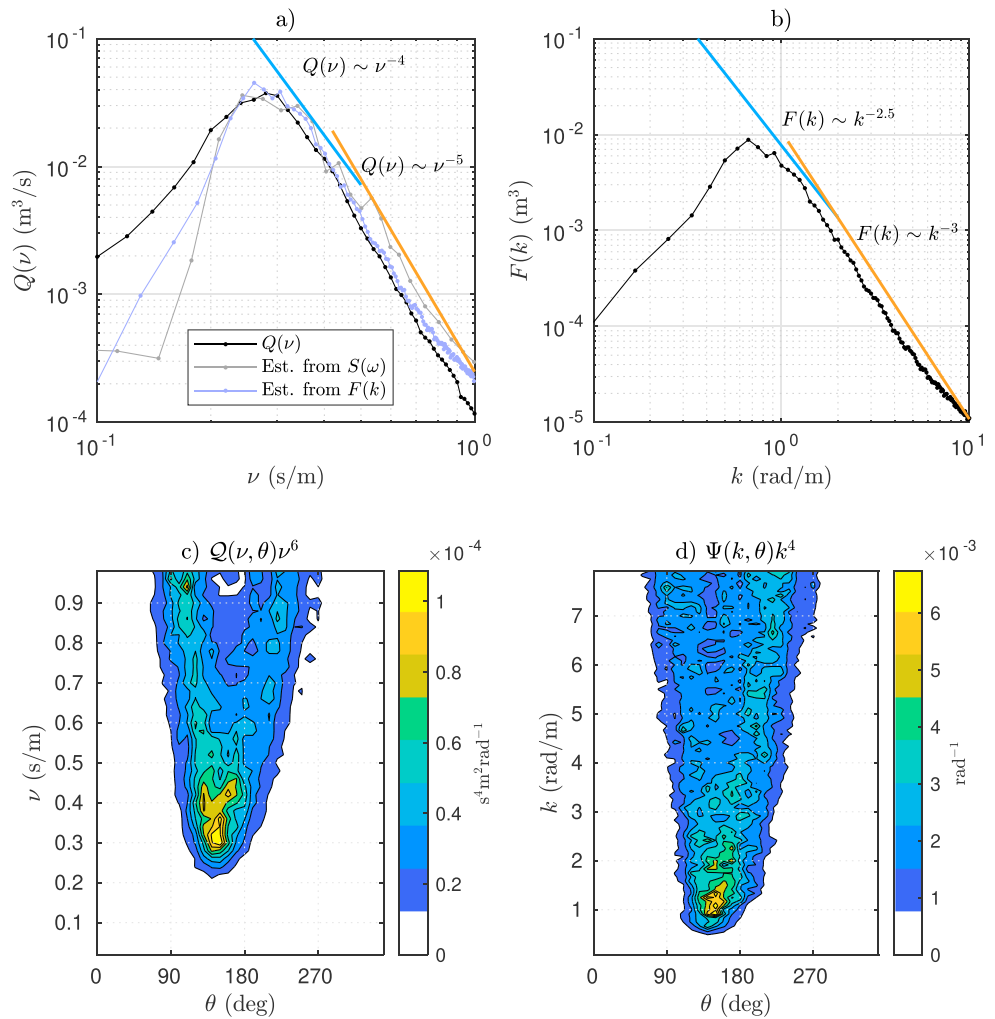


**Figure 10.** The third spectra in Run 15033. (a, c) The omnidirectional and directional inverse phase speed spectra. (b, d) The corresponding wavenumber spectra. Panel (a) also shows the  $Q$ -spectra estimated from  $S(\omega)$  and  $F(k)$  using linear wave theory.

detail in this paper, we still present an example of the directional inverse phase speed spectrum (c) next to the normal directional wavenumber spectrum (d). The spectrum shows a similar bimodal characteristic that has previously been found for wavenumber spectra (e.g., Hwang et al., 2000).

We will now present data from four runs gathered under various conditions.

#### 4.4.1. Run 15033: Strongly Forced Fetch Limited

The noise of the higher wavenumber (Figure 11b) is also visible in the  $Q$ -spectrum (a). The general shape of the  $Q$ -spectrum resembles that of the frequency spectrum because of the similar equilibrium normalization, but the possible second power law transition—which takes place at  $\tilde{\omega} = 10$  in the frequency spectrum—is masked by noise in the  $Q$ -spectrum.

The  $Q$ -spectrum differs from the frequency spectrum especially in two aspects. First, in the  $Q$ -spectrum the power law in the assumed saturation range follows a  $\nu^{-5}$  form closely, while the  $\omega^{-5}$  part in the frequency spectrum is distorted. The saturation level in the  $Q$ -spectrum is also close to twice that of the wavenumber domain, as is expected from theory; in the frequency spectrum this is not the case. (The individual frequency spectra are compatible with the saturation value of  $\alpha \approx 2.5 \cdot 10^{-3}$  that was deduced from the averaged spectra in Figure 9.) Second, the equilibrium values of the different  $Q$ -spectra collapse around  $3 \cdot 10^{-3}$ , while the frequency equilibrium values have a larger spread (roughly  $3\text{--}4.5 \cdot 10^{-3}$ ). As a consequence, the equilibrium-to-saturation transition point also varies more in the frequency spectrum compared to the  $Q$ -spectrum.

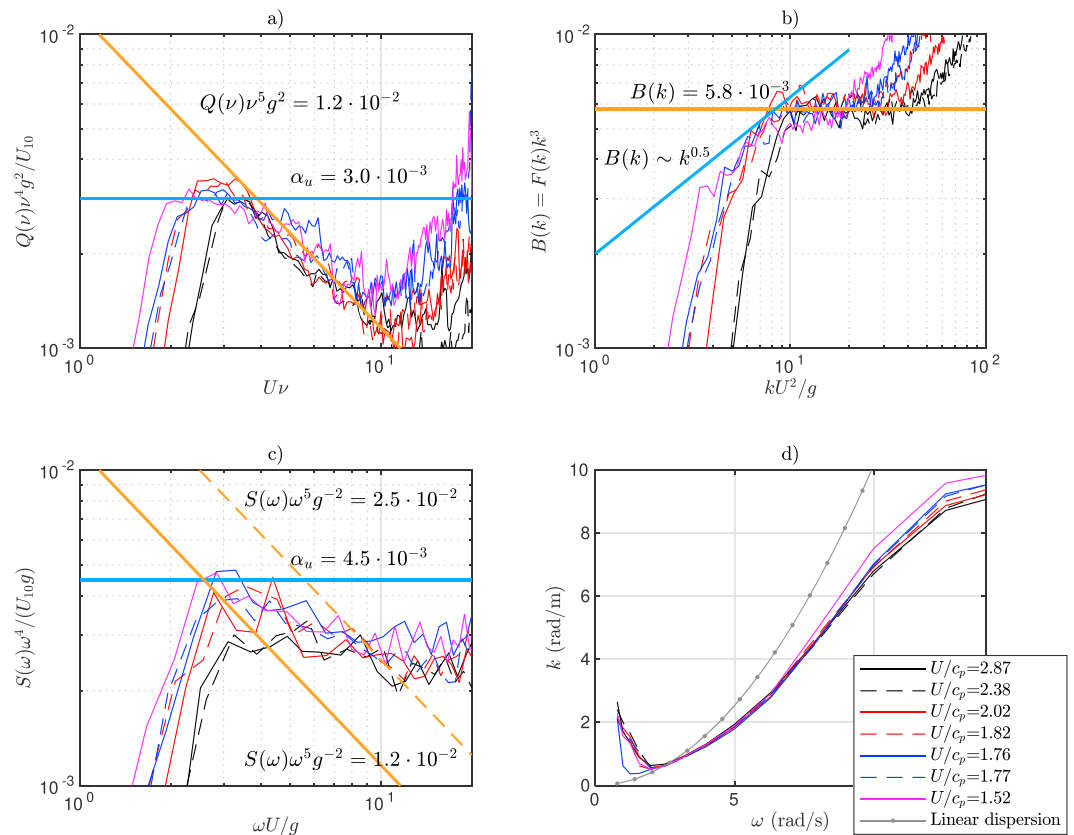


**Figure 11.** The wave spectra from Run 15033. The equilibrium spectra are shown for the inverse phase speed and frequency (a) and the frequency spectra (c), while the saturation spectrum are shown for the wavenumber (b). The mean dispersion relation for all the spectra are shown in panel (d).

The inconsistencies in the frequency spectra seem to depend on the strength of the forcing. The first two spectra—solid and dashed black—are most strongly forced with  $U/c_p$  over 2. These spectra have the lowest equilibrium levels (around  $3 \cdot 10^{-3}$ ). They also seem to transition to the saturation range at a higher dimensionless frequency, around  $\tilde{\omega} = 8$ ; the transition for the last spectra, with  $U/c_p = 1.4$ , happens around  $\tilde{\omega} = 4$ . A similar strong pattern in the transition point is absent in the  $Q$ -spectra, although some variation exists.

In Figure 9 the frequency spectra—averaged according to wind speed bins—showed a power law decaying slower than  $\omega^{-5}$ . Still, the individual spectra in Figure 11c seem to follow an  $\omega^{-5}$  power law more closely than the spectral average. The deviation from the  $\omega^{-5}$  is partially explained as an artifact of the averaging process caused by the variations in equilibrium levels and transition points when the frequency spectra was determined as a function of the dimensionless frequency,  $\tilde{\omega}$ . Nevertheless, even for individual spectra the  $\nu^{-5}$  regime is more clear than to the corresponding  $\omega^{-5}$  region—the averaging artifact is therefore only a partial explanation.

The mean dispersion curves in Figure 11d differ between the different spectra in such a way that a stronger forcing is connected to a greater deviation from the theoretical linear dispersion curve. A stronger  $U/c_p$  forcing produces steeper waves, thus increasing the amount of energy recorded at higher-frequency harmonics. The leakage to higher frequencies also partially overlap with the saturation range, thus distorting the  $\omega^{-5}$  power law in the frequency domain, as determined by Janssen (2009).

#### 4.4.2. Run 15031: Swell and Turning Winds

For the first two spectra the wind sea peaks are visible above the lower frequency,  $240^\circ$ , southwestern swell. After the wind turned to the southeast the individual spectra were very flat and the wind sea cannot clearly be separated from the swell in the omnidirectional spectra (Figure 12d).

The first two spectra that were measured before the wind had turned had power law transitions at about  $U\nu = 3$  in the inverse phase speed spectra, and a similar transition can be identified in the wavenumber

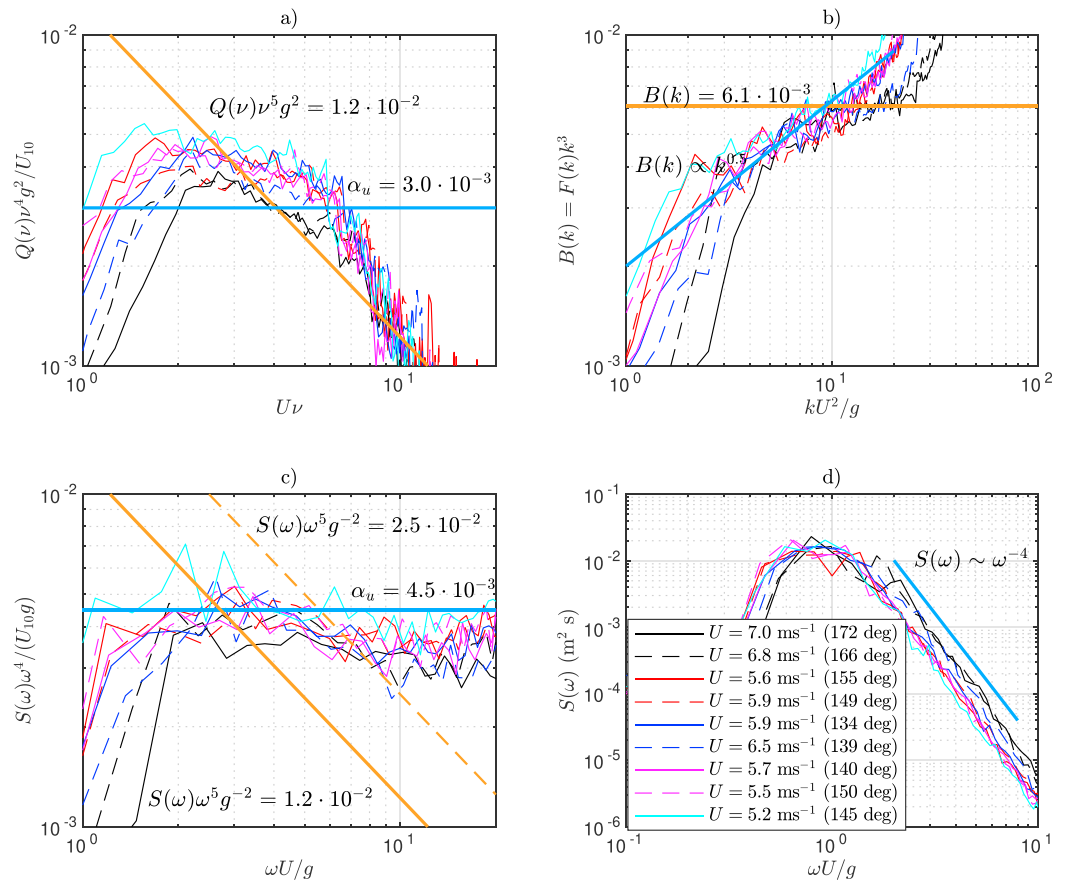


**Figure 12.** The wave spectra from Run 15031 ( $U/c_p > 0.8$ ). The equilibrium spectra are shown for the inverse phase speed and frequency (a) and the frequency spectra (c), while the saturation spectra are shown for the wavenumber (b). The normal frequency spectra are shown in panel (d).

domain. In the frequency domain a transition exist at around  $\tilde{\omega} = 5$ , but it is relatively weak (although consistent with the saturation level determined value from the entire data set). After the wind has turned, the wind sea was fetch limited. The fetch-limited  $Q$ -spectra could easily be interpreted to have a long  $\nu^{-4}$  range, but they can also be viewed as having a transition at roughly  $U\nu=3$ , the spectra after the transition point just decays slower than  $\nu^{-5}$ . The slower decay is also visible in the frequency domain (c).

The slow decay and higher equilibrium levels in the  $Q$ -spectra (compared to Run 15033) would then be explained by the background swell. The slower decay of the tail could also, in theory, be caused by an opposing ambient current (see Appendix B). This is not supported by the data, because an opposing current would simultaneously cause the frequency spectra to decay more rapidly than  $\omega^{-5}$  in the saturation range.

#### 4.4.3. Run 15035: Duration Limited

There is no direct connection between a duration-limited and fetch-limited wave field, since in a duration-limited case all wave components are governed by their own “fetch.” Looking at the individual wavenumber saturation spectra (Figure 13b), they can be interpreted to have an equilibrium-to-saturation transition at  $\tilde{k} \approx 4$ . After a lower saturation level of about  $4.5 \cdot 10^{-3}$  the spectra decays slower.

This interpretation of a “saturation-to-equilibrium” transition is supported by the inverse phase speed spectra (d). The second transitions also explains the difficulties to interpret the mean spectra in Figure 7c and the contradiction between the higher saturation value determined from the averaged spectra.

Figure 13a shows the equilibrium  $Q$ -spectra, which have a very short  $\nu^{-4}$  range (if any) that transitions into a  $\nu^{-5}$  range. The saturation level determined from the  $Q$ -spectra are slightly below the value determined from the wavenumber spectra (Figure 13d), which is possibly caused by currents. The assumed saturation range is followed by a long  $\nu^{-4}$  tail in a similar fashion what is seen in the frequency domain (Figure 13c).

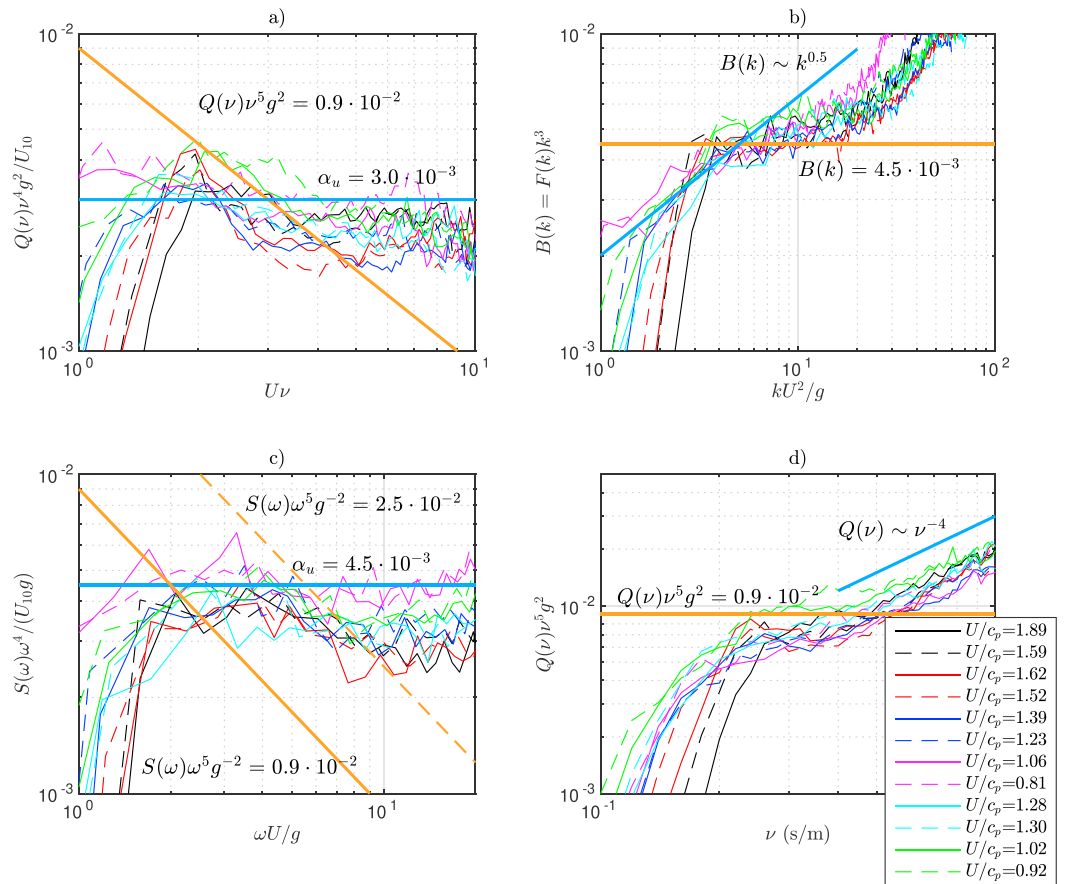


**Figure 13.** The wave spectra from the duration-limited Run 15035. The equilibrium spectra are shown for the inverse phase speed (a) and the frequency spectra (c). The saturation spectra are showed for the wavenumber (b) and the inverse phase speed domain (d).

The frequency spectra have an identifiable  $\omega^{-4}$  range extending to approximately  $\tilde{\omega}=5$ , and a somewhat unclear transition to an  $\omega^{-5}$  range. The  $\omega^{-4}$  transition at  $\tilde{\omega}=10$  is not a product of measurement noise, since the frequency measurements are made with a single wave staff. Similar  $\nu^{-4}$  and  $k^{-2.5}$  subranges (from  $U\nu = 3-4$  and  $\tilde{k} \approx 10$ ) are also visible in the inverse phase speed and wavenumber domain. The end of the ranges are still probably tainted by high wavenumber noise, and the possible connection between these higher subranges is therefore left undetermined.

#### 4.4.4. Run 15044: Weak Winds With Aligned Swell

Run 15044 had very weak winds ( $U = 3$  m/s) growing waves on top of a dominant swell with the same direction. An  $\omega^{-4}$  range is visible in the frequency domain despite both the wavenumber and the inverse phase speed spectra show only a saturation range (Figure 14) with saturation coefficients resembling the lower value determined from the duration-limited Run 15035.

The frequency spectra follow a typical  $\omega^{-4}$  shape with a power law transition at roughly  $\tilde{\omega} = 5$  despite this feature being absent in the other two spectral domains. The wave nonlinearities seem to have an ability to create this type frequency spectra in a wide variety of conditions. The apparent equilibrium level in the frequency spectrum is higher than previous values from the literature, which might be caused by the background swell.

## 5. Discussion

Determining the phase speed of waves is not trivial, since it varies over time periods clearly shorter than what is typically used to calculate wave spectra (e.g., Fedele, 2014; Melville, 1983). Using a long time series to determine one phase speed for a wave component is therefore clearly inadequate. If full spatiotemporal data

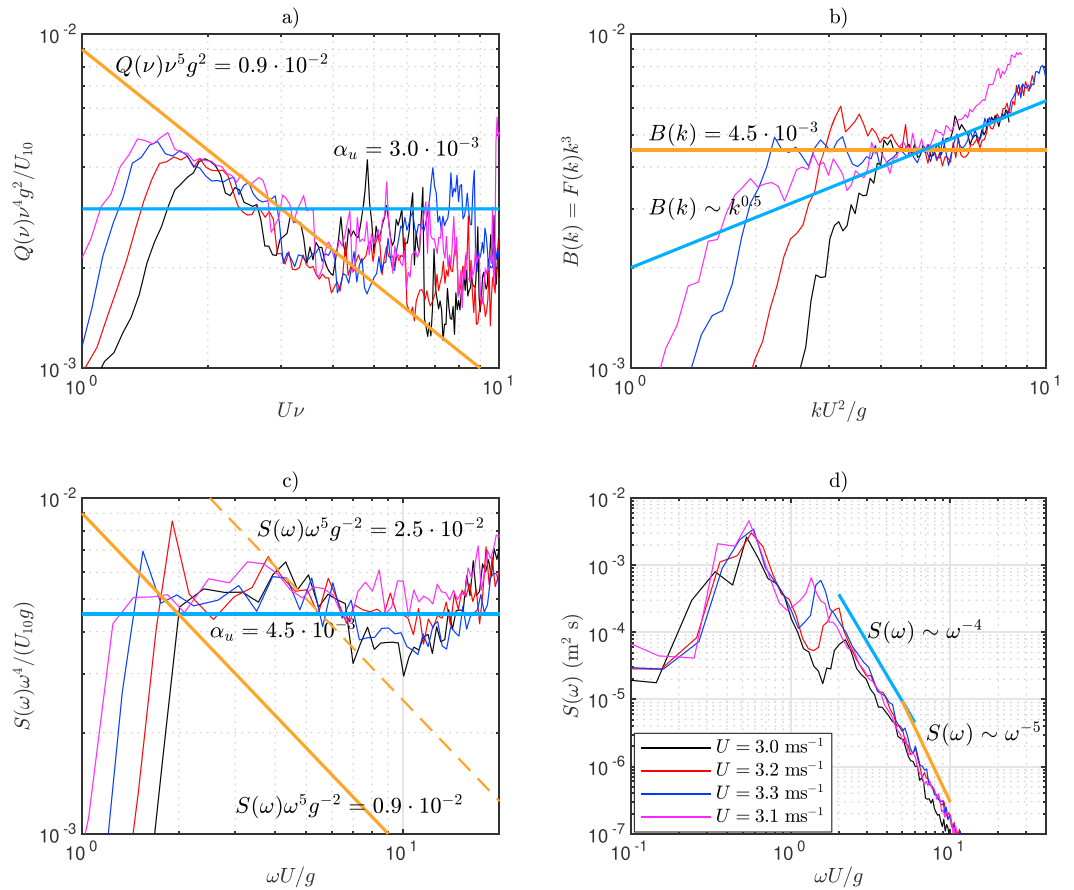


**Figure 14.** The wave spectra from Run 15044 with a wind speed of at least 3 m/s. The equilibrium spectra are shown for the inverse phase speed and frequency (a) and the frequency spectra (c), while the saturation spectra is showed for the wavenumber domain (b). The normal frequency spectra are shown in panel (d).

are available, a 3-D Fourier transform can be applied. In the case of wave staff measurements, some kind of nonstationary analysis must be used, as in Melville (1983). In this paper we adopted the WDM, following Donelan et al. (1996). The main challenge is determining the wavenumber as a function of frequency and time,  $k(\omega, t)$ , since the (inverse) phase speed is then straightforwardly given as  $k(\omega, t)/\omega$ . The suitability of the WDM to calculate inverse phase speed spectra therefore relies on the ability to determine wavenumber spectra.

While the WDM can resolve similar frequency waves with different wave numbers, it will also—if two waves transit the array simultaneously—average two waves to one, thus assigning it a wavenumber in between and biasing the wavenumber estimate low. As noted by Donelan et al. (2015), such an artifact produces a too narrow directional distribution, but it will also cause lower saturation levels in the high wavenumber tail. This behavior seems like a plausible explanation to why the saturation levels determined using the WDM obtained in this paper ( $\approx 5\text{--}6 \cdot 10^{-3}$ ) and by Tamura et al. (2014;  $\approx 4\text{--}5 \cdot 10^{-3}$ ) are slightly lower than those of Lenain & Melville (2017;  $\approx 7 \cdot 10^{-3}$ ), Romero & Melville (2010;  $\approx 8 \cdot 10^{-3}$ ), and Leckler et al. (2015;  $\approx 10 \cdot 10^{-3}$ ). Nevertheless, some scatter is naturally expected because of the variations in wave and wind conditions, and with this in mind our results agree well with previous research.

Assuming a universal saturation range, the transition frequency is determined by the equilibrium constant  $\alpha_u$ . The constant  $\alpha_u$  in the formulation by Kahma (1981) then necessarily leads to a fixed dimensionless transition frequency  $\tilde{\omega}_g = \omega_g U/g = \alpha/\alpha_u$ , where  $\alpha$  is Phillips' saturation range constant (see Appendix A). Donelan et al. (1985) noted that even though the constant  $\alpha_u$  of Kahma (1981) explained the data well in the range they were determined, it could not be comfortably extrapolated to account for the new data in their study. The authors therefore proposed that  $\alpha_u$  of the equilibrium range is not universal but depends

on the strength of the forcing,  $U/c_p$ . Also, the varying transition frequencies of Kahma and Calkoen (1992) can be seen to suggest a nonconstant value for  $\alpha_u$  in the frequency spectrum. Our frequency data were best explained by a constant saturation range combined with an equilibrium range that depended on the inverse wave age.

The equilibrium-range properties of the frequency spectra in our strongly forced fetch-limited case depended on the strength of the forcing, while the inverse phase speed spectra showed smaller variations (Figure 11). The leading explanation for the differences cannot be the Doppler shift (as proposed by Kitaigorodskii et al., 1975, and Banner, 1990), since it would also distort the saturation subrange of the  $Q$ -spectra, thus leading to an inconsistency with the wavenumber spectra (see Appendix B). We conclude that the decrease in the frequency equilibrium level—and increase in the transition frequency—is mostly an artifact of steeper waves generated by a stronger forcing; hence, it is questionable to which extent this dependence on the forcing can be seen as a fundamental property of the wave field. The wave nonlinearities can also seemingly create an  $\omega^{-4}$  range without any counterpart in the wavenumber or inverse phase speed domain (Figure 14).

Our observations offer more direct experimental evidence that wave nonlinearities, not the Doppler shift, is the leading cause in the distortion of the high-frequency part of the spectrum. The good agreement between the saturation ranges of the wavenumber and inverse phase speed spectrum also gives experimental confirmation for the theoretical results of Janssen (2009) that the contributions of the wave nonlinearities are small in the wavenumber domain. We also note, that an inverse phase speed spectrum decaying as  $\nu^{-5}$  (Figures 11 and 14) would suggest that the first-order spectrum (i.e., the spectrum without higher-order nonlinear effects) decays at an even faster rate, as discussed by Leckler et al. (2015).

A second transition from an  $\omega^{-5}$  to an  $\omega^{-4}$  power law in the frequency measurements is observed consistently, but such short waves are not resolved with complete confidence in the spatial domain. Thus, no comparative analysis could be made. We still note that this transition takes place in the gravity wave regime and is therefore separate from the  $\omega^{-5}$  to  $\omega^{-4}$  transition reported by Mitsuyasu (1977) at frequencies affected by capillary effects. These two transitions together create frequency spectra that have an apparent continuous  $\omega^{-4}$  power law, but with a slightly lower equilibrium level for the highest frequencies. Such a spectrum is visible also in Lenain & Melville (2017, their Figure 7), where this shift happens around  $f = 0.6$  Hz (roughly  $\omega U/g = 4$ ). If the spectrum ends before the second transition takes place, one might interpret the spectrum to simply have a transition to an  $\omega^{-5}$  regime (e.g., Fig 14d).

The wavenumber data in this study also scaled well with the friction velocity,  $u_*$ , as was also found by Lenain and Melville (2017). The friction velocity is therefore still a valid candidate to represent the wind conditions, but the physical interpretation of the quantity  $u_*\nu$  is not as immediately attractive or straightforward as  $U\nu$ . One obvious usage of the inverse phase speed spectrum would be in quantifying the momentum flux from the wind to the waves, since the central quantity  $U/c$  is directly captured for each wave component without the need for any additional current measurements or corrections. If quality current measurements are available, the difference between the wavenumber spectrum and the  $Q$ -spectrum could also be used to study the effect of the Doppler shift over different scales, since it can be accounted for in the  $Q$ -spectrum without any additional assumptions about wave dispersion (see Appendix B). On the other hand, the wavenumber spectrum is the proper tool to quantify, for example, wave dissipation, which depends on intrinsic properties, such as the wave steepness.

The directional distribution for higher-frequency/wavenumber waves becomes more complicated, and its exact shape is still not known (Donelan et al., 1985, 2015; Hwang et al., 2000; Hwang & Wang, 2001; Leckler et al., 2015; Peureux et al., 2018; Young et al., 1995). Expectedly, signs of a deviation from a standard unimodal distribution is also found in our data (Figure 5 and 10). Integrating over all directions and calculating the dimensionless phase speed  $U\nu$  from the modulus  $\nu = |\nu|$  might therefore not be optimal, but we nevertheless chose this approach to allow for a fair comparison to, for example, the omnidirectional wavenumber spectrum. Donelan et al. (1985) scaled his spectra using the wind component in the direction of the spectral peak, but from the point of view of the  $Q$ -spectrum the relevant wind speed have to be calculated in the direction of each wave component separately. Nevertheless, such detailed information of the directional

inverse phase speed distribution might be beyond what can be extracted from wave staff measurements using the WDM.

## 6. Conclusions

High-frequency wave data from R/V *Aranda* were presented and the spectra compared well to measurements from a nearby wave buoy. We used the WDM to extract both the frequency and the wavenumber of wave components from data recorded by five wave staffs.

The main contribution of this paper is the introduction of a new wave spectrum,  $Q(\nu)$  ( $\text{m}^3/\text{s}$ ), where  $\nu = c^{-1} = k\omega^{-1}$  is the inverse phase speed. Determining this spectrum is only meaningful from explicit frequency-wavenumber data that eliminate the need for any assumptions concerning the wave dispersion. Using the linear dispersion relation to determine  $\nu = \omega g^{-1}$  would only lead to a trivial rescaling of the frequency spectrum. The  $Q$ -spectrum has the following saturation range and equilibrium range:

$$Q(\nu) \sim \alpha g^{-2} \nu^{-5} \quad (20)$$

$$Q(\nu) \sim \alpha_u U g^{-2} \nu^{-4}, \quad (21)$$

where  $\alpha$  (Phillips, 1958) and  $\alpha_u$  (Kahma, 1981) are the same constants that are normally used to describe the subranges of the frequency spectrum.

We studied the properties of this spectrum for different locations and wave conditions in the Baltic Sea. When it could be determined, the saturation value for the  $Q$ -spectrum was roughly  $1 \cdot 10^{-2}$ . This was close to twice the saturation value calculated from the wavenumber spectra, which is expected from theory. The saturation range in the frequency spectra was less pronounced, decayed slower than  $\omega^{-5}$ , and had a higher saturation value or about  $\alpha = 2.5 \cdot 10^{-2}$ , thus being inconsistent with the other spectral domains. We determined that the effect of the Doppler shift in our results was small, since it would have otherwise broken the observed similarity of the saturation ranges in the  $Q$ -spectra and the wavenumber spectra. With this uncertainty removed, we deduced that the main explanation for the variations and inconsistencies in the frequency spectra were caused by the presence of nonlinear harmonic components, which is in line with recent studies (Guimarães, 2018; Leckler et al., 2015).

During a strongly forced ( $U/c_p = 2-3$ ) fetch-limited case the equilibrium levels,  $\alpha_u$ , in the frequency spectrum varied with the strength of the forcing; such a variation was practically absent in the  $Q$ -spectrum (Figure 11). The saturation range in the inverse phase speed and frequency domain decayed slower than  $\nu^{-5}$ , and  $\omega^{-5}$ , respectively, when a swell propagating with an 90–100° angle with respect to a fetch-limited wind sea (Figure 12). When it could be determined, the equilibrium-to-saturation transition took place slightly above  $U\nu = 3$ .

In duration-limited cases, with and without swell, the  $Q$ -spectra were mostly characterized by a  $\nu^{-5}$  rear face, while the frequency spectra showed an equilibrium range and a transition at roughly  $\tilde{\omega} = 5$  (Figure 13 and 14). Nonetheless, the duration-limited spectra with higher winds still did not show clear subranges and transitions in the wavenumber and inverse phase speed domains.

The wavenumber spectrum is fundamentally correct if the intrinsic nature of the waves, such as the wave steepness, is the main interest. The new inverse phase speed spectrum can offer a more straightforward representation of the waves if the central parameter is the apparent speed of the waves, with the most obvious example being the study of the momentum transfer between the wind and the waves. In such cases  $U\nu = U/c$  is given directly by the  $Q$ -spectrum without separate current measurements and theoretical assumptions regarding the Doppler shift or velocity bunching.

## Appendix A: Connection Between Equilibrium Levels and Transition Frequency

The saturation range of the spectrum of Phillips (1958)—valid above some yet undetermined frequency  $\omega_g$ —is of the form

$$S(\omega) = \alpha g^2 \omega^{-5}, \quad (A1)$$

where  $\alpha$  is a constant.

The equilibrium spectrum of Kahma (1981)—valid on the rear face of the spectrum prior to the Phillips' range—is of the form

$$S(\omega) = \alpha_u U g \omega^{-4}, \quad (\text{A2})$$

where  $\alpha_u = 4.5 \cdot 10^{-3}$  is a constant. Donelan et al. (1985) presented the equilibrium range of the spectrum in a form derived from the spectrum by Phillips (1958) by exchanging a frequency for the peak frequency:

$$S(\omega) = \alpha_D g^2 \omega_p^{-1} \omega^{-4}. \quad (\text{A3})$$

In this expression  $\alpha_D$  is not a constant but was given as a function of the wave age as

$$\alpha_D = \alpha_u (U/c_p)^p, \quad (\text{A4})$$

where  $\alpha_u$  is a constant and  $p$  is a real number. Donelan et al. (1985) proposed  $\alpha_u = 6 \cdot 10^{-3}$  and  $p = 0.55$ . With a choice of  $\alpha_u = 4.5 \cdot 10^{-3}$  and  $p = 1$  the formulation is equivalent to that of Kahma (1981), since

$$S(\omega) = (\alpha_u U/c_p) g^2 \omega_p^{-1} \omega^{-4} = (\alpha_u U \omega_p g^{-1}) g^2 \omega_p^{-1} \omega^{-4} = \alpha_u U g \omega^{-4}. \quad (\text{A5})$$

If we want to introduce the wave age dependent  $\alpha_u$  in the spectrum by Kahma (1981), we get

$$S(\omega) = \alpha_u (U/c_p)^{p-1} U g \omega^{-4}, \quad (\text{A6})$$

where  $p$  is the same exponent as used by Donelan et al. (1985).

The transition frequency,  $\omega_g$ , is defined as the point when the equilibrium range meets the saturation range:

$$\alpha_u (U/c_p)^{p-1} U g \omega_g^{-4} = \alpha g^2 \omega_g^{-5} \quad (\text{A7})$$

$$\frac{\omega_g U}{g} = \frac{\alpha}{\alpha_u} \left( \frac{U}{c_p} \right)^{1-p}. \quad (\text{A8})$$

It is easy to see that for the expression of Kahma, (1981;  $p = 1$ ), where the equilibrium range depends linearly on the wind speed, the dimensionless transition frequency,  $\tilde{\omega}_g$ , is constant. For a choice of  $p = 0$  the direct wind speed dependence vanishes, and we get

$$\frac{\omega_g U}{g} = \frac{\alpha}{\alpha_u} \left( \frac{U}{c_p} \right)^1 \quad (\text{A9})$$

$$\frac{\omega_g U}{g} = \frac{\alpha}{\alpha_u} \left( \frac{U \omega_p}{g} \right) \quad (\text{A10})$$

$$\frac{\omega_g}{\omega_p} = \frac{\alpha}{\alpha_u}. \quad (\text{A11})$$

In other words, the transition frequency is always a constant multiple of the peak. The equilibrium range is then not a function of the wind speed, but depends only on the peak frequency (which in turn has a dependence on the wind speed). Expressed in terms of the spectrum of Donelan et al. (1985), the case  $p = 0$  would mean that the constant  $\alpha_D$  is a constant independent of the forcing—a direct analogue to the original Phillips' spectrum.

## Appendix B: Doppler Shift of the $Q(\nu)$ Spectrum With an Ambient Current

The intrinsic frequency of a wave is Doppler shifted if a mean current is present. The apparent frequency will then be given by

$$\omega = \sigma + k U_c \cos(\varphi), \quad (\text{B1})$$

where  $\omega$  and  $\sigma$  are the apparent and intrinsic frequencies,  $U_c$  is the current speed, and  $\varphi$  is the angle between the wave and current directions. In the frequency domain the effect of the current on the saturation spectrum has been estimated by assuming that the wavenumbers follow the linear dispersion relation (Kitaigorodskii et al., 1975). If  $\varphi > 0$  (a following current) the saturation spectrum will decay slower than  $\omega^{-5}$  and exhibit higher spectral values (Banner, 1990; Kitaigorodskii et al., 1975).

Since the inverse phase speed spectrum in this paper is calculated from the measured wavenumber and frequency of the wave components, no assumptions about  $k$  have to be made. We can therefore simply multiply equation (B1) with  $k^{-1}$ :

$$\frac{\omega}{k} = \frac{\sigma}{k} + U_c \cos(\varphi) \quad (\text{B2})$$

$$c = c_\sigma + U_c \cos(\varphi). \quad (\text{B3})$$

The relationship between the intrinsic inverse phase speed,  $v_\sigma = c_\sigma^{-1}$ , and the apparent inverse phase speed,  $v = c^{-1}$ , is now determined by

$$v = \frac{1}{(v_\sigma)^{-1} + U_c \cos(\varphi)}. \quad (\text{B4})$$

The Jacobian of the transformation will be

$$J = \frac{\partial v_\sigma}{\partial v} = \frac{1}{(1 - U_c \cos(\varphi)v)^2}. \quad (\text{B5})$$

Under a following current ( $\varphi > 0$ ) the apparent frequency will increase ( $\omega > \sigma$ ). Since the wavenumber is fixed (instead of being estimated from the frequency), the apparent phase speed will also increase ( $c > c_\sigma$ ). This, again, is equivalent with a decrease in the apparent inverse phase speed ( $v < v_\sigma$ ). As a result, the spectral levels will decrease, thus leading to a lower saturation constant  $\alpha$ .

Such a lowering of the saturation constant is seen in Figure 11a, where the saturation values around  $\alpha = Q(v)\sigma^2 v^5 = 1 \cdot 10^{-1}$  are slightly lower than what is estimated from the pure wavenumber measurements using liner theory ( $\alpha = 1.2 \cdot 10^{-2}$ ). The factor 1.2 difference roughly corresponds to a current speed of  $U_c \cos(\varphi) = 0.1$  m/s (1–2% of the wind speed in Run 15033). The Doppler shift of an ambient current will also affect the power law of the saturation spectrum making it decay slightly faster than  $v^{-5}$ . Nevertheless, this effect is small for such low current speeds.

The Jacobian in equation (B5) becomes infinite in the case of an opposing current with a speed equal to the phase speed of the wave component. While no current measurements are available for this study, the slowest waves captured by the experimental setup are roughly 0.8 m/s. They are therefore faster than even the strong, 0.4 m/s, currents that have been measured in narrow fairways in the Archipelago Sea (Kanarik et al., 2018). Typical current speeds in the Baltic Sea are around 0.1–0.3 m/s. Still, in the case of stronger currents and/or observational techniques capable of resolving slower waves, the singularity issue of the Jacobian can become relevant.

#### Acknowledgments

This work has been funded by Arvid och Greta Olins Fond (Svenska kulturfonden, 17/103386), Finska Vetenskaps-Societeten, and Magnus Ehrnrooths stiftelse. The research has also received funding from BONUS, the joint Baltic Sea research and development program (Art 185) through Grant 03F0773A (BONUS INTEGRAL). We would like to thank the captain and crew of R/V *Aranda* for their flexibility and expertise shown during the expeditions. This study has utilized research infrastructure facilities provided by FINMARI (Finnish Marine Research Infrastructure network). The data are available through its DOI (<https://doi.org/10.5281/zenodo.2516432>). We want to extend our thanks to the anonymous reviewers. Their constructive comments and suggestions allowed us to improve and strengthen this manuscript.

#### References

- Banner, M. L. (1990). Equilibrium spectra of wind waves. *Journal of Physical Oceanography*, 20(7), 966–984. [https://doi.org/10.1175/1520-0485\(1990\)020<0966:ESOWW>2.0.CO;2](https://doi.org/10.1175/1520-0485(1990)020<0966:ESOWW>2.0.CO;2)
- Barrick, D. E., & Weber, B. L. (1977). On the nonlinear theory for gravity waves on the ocean's surface. Part II: Interpretation and applications. *Journal of Physical Oceanography*, 7, 11–21. [https://doi.org/10.1175/1520-0485\(1977\)007<0011:otntfg>2.0.co;2](https://doi.org/10.1175/1520-0485(1977)007<0011:otntfg>2.0.co;2)
- Donelan, M. A., Babanin, A. V., Sanina, E., & Chalikov, D. V. (2015). A comparison of methods for estimating directional spectra of surface waves. *Journal of Geophysical Research: Oceans*, 120, 5040–5053. <https://doi.org/10.1002/2015JC010808>
- Donelan, M. A., Drennan, W. M., & Magnusson, A. K. (1996). Nonstationary analysis of the directional properties of propagating waves. *Journal of Physical Oceanography*, 26(9), 1901–1914. [https://doi.org/10.1175/1520-0485\(1996\)026<1901:NAOTDP>2.0.CO;2](https://doi.org/10.1175/1520-0485(1996)026<1901:NAOTDP>2.0.CO;2)
- Donelan, M. A., Hamilton, J., & Hui, W. H. (1985). Directional spectra of wind-generated waves. *Philosophical Transactions of the Royal Society A: Mathematical, Physical and Engineering Sciences*, 315(1534), 509–562. <https://doi.org/10.1098/rsta.1985.0054>
- Drennan, W. M., Donelan, M. A., Madsen, N., Katsaros, K. B., Terray, E. A., & Flagg, C. N. (1994). Directional wave spectra from a swath ship at sea. *Journal of Atmospheric and Oceanic Technology*, 11(4), 1109–1116. [https://doi.org/10.1175/1520-0426\(1994\)011<1109:DWSFAS>2.0.CO;2](https://doi.org/10.1175/1520-0426(1994)011<1109:DWSFAS>2.0.CO;2)
- Dupuis, H., Guerin, C., Hauser, D., Weill, A., Nacass, P., Drennan, W. M., et al. (2003). Impact of flow distortion corrections on turbulent fluxes estimated by the inertial dissipation method during the FETCH experiment on R/V *L'Atalante*. *Journal of Geophysical Research*, 108(C3), 8064. <https://doi.org/10.1029/2001JC001075>

- Fedele, F. (2014). Geometric phases of water waves. *EPL (Europhysics Letters)*, *107*(6), 224–230. <https://doi.org/10.1209/0295-5075/107/69001>
- Forristall, G. Z. (1981). Measurements of a saturated range in ocean wave spectra. *Journal of Geophysical Research*, *86*(C9), 8075–8084. <https://doi.org/10.1029/JC086iC09p08075>
- Guimarães, P. V. (2018). Sea surface and energy dissipation (Ph.D. thesis), Loire Bretagne University.
- Hara, T., & Karachintsev, A. V. (2003). Observation of nonlinear effects in ocean surface wave frequency spectra. *Journal of Physical Oceanography*, *33*(2), 422–430. [https://doi.org/10.1175/1520-0485\(2003\)033<0422:OONEIO>2.0.CO;2](https://doi.org/10.1175/1520-0485(2003)033<0422:OONEIO>2.0.CO;2)
- Hisaki, Y., & Tokuda, M. (1995). Detection of nonlinear waves and their contribution to ocean wave spectra. Part II: Observation. *Journal of Oceanography*, *51*(4), 407–419. <https://doi.org/10.1007/BF02286388>
- Hwang, P., & Wang, D. W. (2001). Directional distributions and mean square slopes in the equilibrium and saturation ranges of the wave spectrum. *Journal of Physical Oceanography*, *31*(5), 1346–1360. [https://doi.org/10.1175/1520-0485\(2001\)031<1346:DDAMSS>2.0.CO;2](https://doi.org/10.1175/1520-0485(2001)031<1346:DDAMSS>2.0.CO;2)
- Hwang, P., Wang, D. W., Walsh, E. J., Krabill, W. B., & Swift, R. N. (2000). Airborne measurements of the wavenumber spectra of ocean surface waves. Part II: Directional distribution. *Journal of Physical Oceanography*, *30*(11), 2753–2767. [https://doi.org/10.1175/1520-0485\(2001\)031<2753:AMOTWS>2.0.CO;2](https://doi.org/10.1175/1520-0485(2001)031<2753:AMOTWS>2.0.CO;2)
- Janssen, P. (2009). On some consequences of the canonical transformation in the Hamiltonian theory of water waves. *Journal of Fluid Mechanics*, *637*, 1–44. <https://doi.org/10.1017/S0022112009008131>
- Kahma, K. K. (1981). A study of the growth of the wave spectrum with fetch. *Journal of Physical Oceanography*, *11*(11), 1503–1515.
- Kahma, K. K., & Calkoen, C. J. (1992). Reconciling discrepancies in the observed growth of wind-generated waves. *Journal of Physical Oceanography*, *22*(12), 1389–1405. [https://doi.org/10.1175/1520-0485\(1992\)022<1389:RDITOG>2.0.CO;2](https://doi.org/10.1175/1520-0485(1992)022<1389:RDITOG>2.0.CO;2)
- Kanarik, H., Tuomi, L., Alenius, P., Lensu, M., Miettunen, E., & Hietala, R. (2018). Evaluating strong currents at a fairway in the Finnish Archipelago Sea. *Journal of Marine Science and Engineering*, *6*(122), 1–20. <https://doi.org/10.3390/jmse6040122>
- Kitaigorodskii, S. A. (1983). On the theory of the equilibrium range in the spectrum of wind-generated gravity waves. *Journal of Physical Oceanography*, *13*(5), 816–827. [https://doi.org/10.1175/1520-0485\(1983\)013<0816:OTTOTE>2.0.CO;2](https://doi.org/10.1175/1520-0485(1983)013<0816:OTTOTE>2.0.CO;2)
- Kitaigorodskii, S. A., Krasitskii, V. P., & Zaslavskii, M. M. (1975). On Phillips' theory of equilibrium range in the spectra of wind-generated gravity waves. *Journal of Physical Oceanography*, *5*(3), 410–420. [https://doi.org/10.1175/1520-0485\(1975\)005<0410:OPTOER>2.0.CO;2](https://doi.org/10.1175/1520-0485(1975)005<0410:OPTOER>2.0.CO;2)
- Komen, G. J. (1980). Nonlinear contribution to the frequency spectrum of wind-generated water waves. *Journal of Physical Oceanography*, *10*, 779–790.
- Leckler, F., Ardhuin, F., Peureux, C., Benetazzo, A., Bergamasco, F., & Dulov, V. (2015). Analysis and interpretation of frequency-wavenumber spectra of young wind waves. *Journal of Physical Oceanography*, *45*(10), 2484–2496. <https://doi.org/10.1175/JPO-D-14-0237.1>
- Lenain, L., & Melville, W. K. (2017). Measurements of the directional spectrum across the equilibrium-saturation ranges of wind-generated surface waves. *Journal of Physical Oceanography*, *47*, 17–0017. <https://doi.org/10.1175/JPO-D-17-0017.1>
- Lund, B., Collins III, C. O., Tamura, H., & Graber, H. C. (2016). Multi-directional wave spectra from marine X-band radar. *Ocean Dynamics*, *66*(8), 973–988. <https://doi.org/10.1007/s10236-016-0961-z>
- Melville, W. K. (1983). Wave modulation and breakdown. *Journal of Fluid Mechanics*, *128*, 489–506. <https://doi.org/10.1017/S0022112083000579>
- Mitsuyasu, H. (1977). Measurement of the high-frequency spectrum of ocean surface waves. *Journal of Physical Oceanography*, *7*(6), 882–891. [https://doi.org/10.1175/1520-0485\(1977\)007<0882:MOTHFS>2.0.CO;2](https://doi.org/10.1175/1520-0485(1977)007<0882:MOTHFS>2.0.CO;2)
- Peureux, C., Benetazzo, A., & Ardhuin, F. (2018). Note on the directional properties of meter-scale gravity waves. *Ocean Science*, *14*, 41–52. <https://doi.org/10.5194/os-14-41-2018>
- Phillips, O. M. (1958). The equilibrium range in the spectrum of wind-generated waves. *Journal of Fluid Mechanics*, *4*(4), 426–434. <https://doi.org/10.1017/S0022112058000550>
- Phillips, O. M. (1985). Spectral and statistical properties of the equilibrium range in wind-generated gravity waves. *Journal of Fluid Mechanics*, *156*, 505–531. <https://doi.org/10.1017/S0022112085002221>
- Romero, L., & Melville, W. K. (2010). Airborne observations of fetch-limited waves in the Gulf of Tehuantepec. *Journal of Physical Oceanography*, *40*(3), 441–465. <https://doi.org/10.1175/2009JPO4127.1>
- Tamura, H., Drennan, W. M., Sahlée, E., & Graber, H. C. (2014). Spectral form and source term balance of short gravity wind waves. *Journal of Geophysical Research: Oceans*, *119*, 7406–7419. <https://doi.org/10.1002/2014JC009869>
- Toba, Y. (1973). Local balance in the air-sea boundary processes—III. On the spectrum of wind waves. *Journal of the Oceanographical Society of Japan*, *29*, 209–220. <https://doi.org/10.1007/BF02108528>
- Wang, D. W., & Hwang, P. (2004). The dispersion relation of short wind waves from space-time wave measurements. *Journal of Atmospheric and Oceanic Technology*, *21*(12), 1936–1945. <https://doi.org/10.1175/JTECH-1669.1>
- Young, I. R., Verhagen, L. A., & Banner, M. L. (1995). A note on the bimodal directional spreading of fetch-limited wind waves. *Journal of Geophysical Research*, *100*(C1), 773–778. <https://doi.org/10.1029/94JC02218>